e-ISSN: 3023-6487

JRM

Journal of Radiology in Medicine

Volume: 3

Issue: 3

Year: 2026

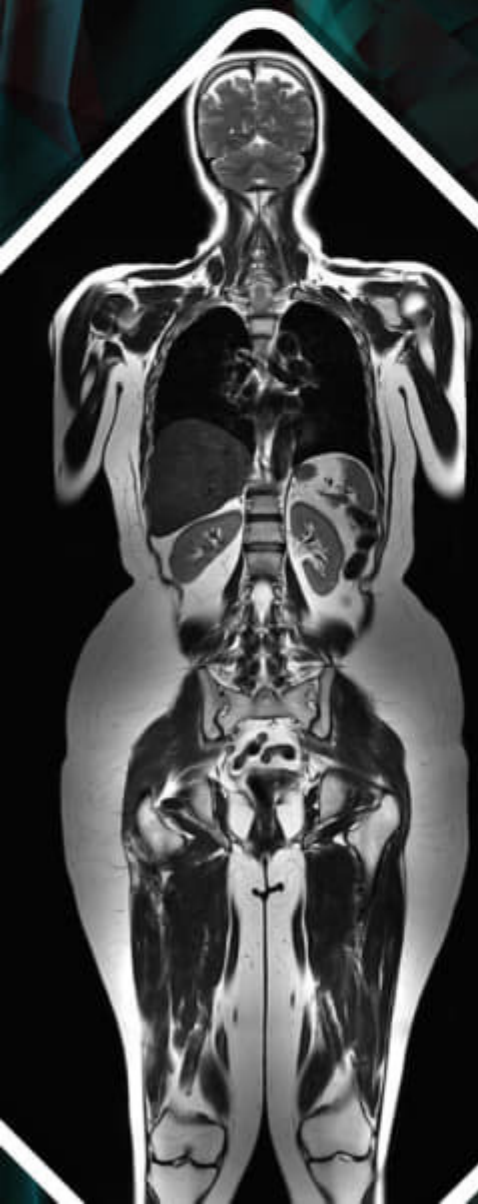

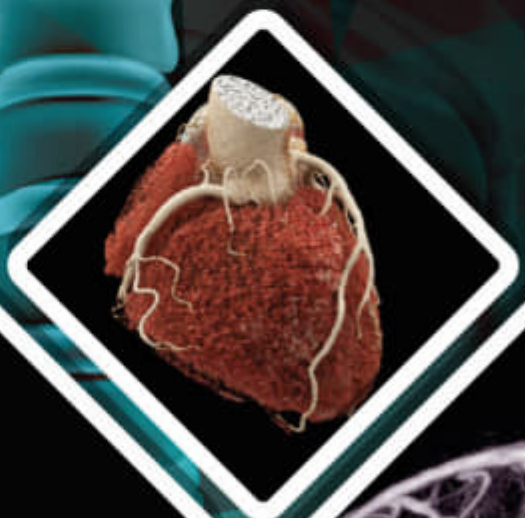

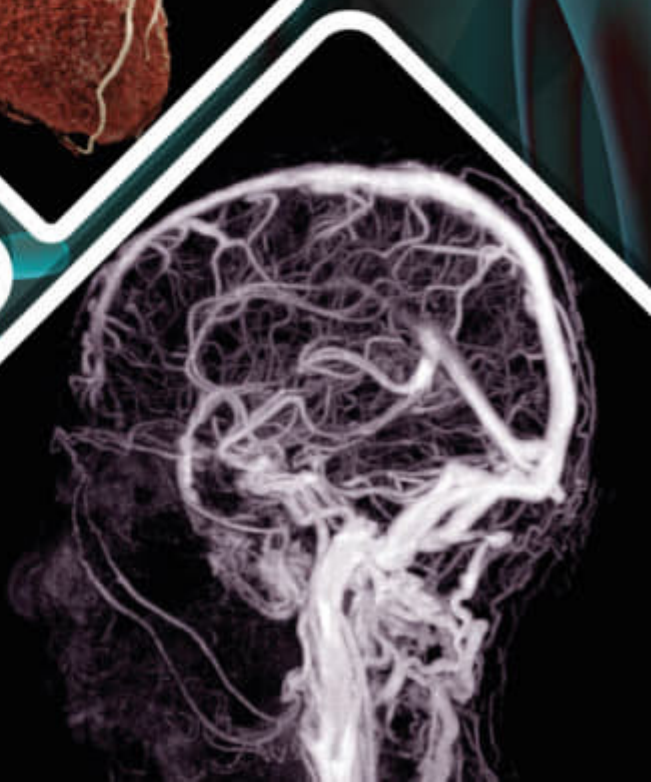

MHA
MEDIHEALTH ACADEMY

Journal of Radiology in Medicine

Editorial Board

EDITORS-IN-CHIEF

ASSOCIATE EDITOR-IN-CHIEF

EDITORIAL BOARD

Journal of Radiology in Medicine

Contents

Volume: 3 Issue: 3 Year: 2026

ORIGINAL ARTICLES

CASE REPORTS

Journal of Radiology Medicine in

Original Article

Doi: 10.51271/JRM-0051

Comparison of chatbots for patient information on head and neck imaging techniques in terms of scientific quality and readability

Meltem Horoz*[1], Ayşegül Cavnar[2]

[1]Department of Oral and Maxillofacial Radiology, Faculty of Dentistry, Kırıkkale University, Kırıkkale, Turkiye
[2]Department of Prosthodontics, Faculty of Dentistry, Gazi University, Ankara, Turkiye

Received: 15.06.2026 ◆ **Accepted**: 17.08.2026 ◆ **Published**: 19.09.2026

Cite this article: Horoz M, Cavnar A. Comparison of chatbots for patient information on head and neck imaging techniques in terms of scientific quality and readability. *J Radiol Med.* 2026;3(3):54-58. doi:10.51271/JRM-0051

***Corresponding Author:** Meltem Horoz, meeltemhoroz@hotmail.com

ABSTRACT

Aims: This study aimed to evaluate the scientific quality and readability of the responses of ChatGPT and Microsoft Copilot to patient questions about head and neck imaging methods in dentistry.

Methods: Twenty patient-focused questions were directed to both chatbots. Responses were evaluated independently by two experts using a 7-point Likert scale, and readability levels were analyzed using the Flesch Reading Ease Score and Flesch-Kincaid Grade Level (FKGL) indices. Inter-expert agreement was assessed using Cohen's Kappa, and differences between chatbots were assessed using an independent-samples t-test.

Results: Statistically significant but weak agreement was observed among experts (κ=0.399, $p<0.001$). No significant difference was found between ChatGPT and Microsoft Copilot in terms of Flesch Reading Ease Score index and expert scores ($p>0.05$). However, FKGL scores were significantly higher in Microsoft Copilot ($p=0.025$), indicating more linguistically complex responses.

Conclusion: ChatGPT and Microsoft Copilot demonstrated similar scientific quality and readability based on FRES scores. However, Microsoft Copilot generated more linguistically complex responses than ChatGPT, as reflected by its significantly higher FKGL scores, indicating that a higher educational level may be required for comprehension. In conclusion, AI-based chatbots can be useful as supportive tools in patient information and education, but expert supervision remains crucial in this area.

Keywords: Artificial Intelligence, chatbots, patient education as topic, radiologic health

INTRODUCTION

Artificial Intelligence (AI) is a set of technologies that enable computer systems to perform various tasks by mimicking human cognitive abilities. These systems can learn from data, analyze information, and generate appropriate outputs. They can exhibit functions similar to human intelligence in processes such as decision-making and problem-solving.[1] Large language models (LLMs) are AI systems trained with data from articles, books, and online resources. These models utilize deep learning-based neural network architectures to model complex connections between words in textual data.[2] LLMs use deep learning techniques to process language, enabling them to perform a wide range of tasks such as translation, summarizing, and answering questions. Their ability to produce coherent and meaningful texts makes them valuable tools in fields like education and healthcare. Research has shown that LLMs also help medical professionals and patients access and interpret large amounts of data efficiently and accurately. By providing information quickly, they can improve patient care and education and contribute to the medical workflow.[3] Among LLMs, chatbots are conversational AI systems capable of simulating human-like conversation through text and voice. Thanks to their natural language processing capabilities, a subfield of AI, chatbots can understand and answer human questions. One of the key features of chatbots in the healthcare field is their ability to provide accessible information to users by managing data and answering specific, focused questions.[4] In November 2022, OpenAI (San Francisco, USA) introduced the Chat Generative Pre-trained Transformer (ChatGPT). This LLM, which combines AI and natural language processing technologies, can analyze dialogues and generate appropriate response texts.[5] Numerous studies have evaluated

the performance of chatbots in various medical specialties. In particular, ChatGPT's successful performance on the United States Medical Licensing Exam without additional training has highlighted the potential of AI-based chatbots in medicine and increased interest in their use in healthcare. In dentistry, studies evaluating chatbot performance have increased since 2023, with studies conducted across specialties such as general dentistry, periodontology, orthodontics, and oral, dental, and maxillofacial surgery.[6] Although there are studies in the literature examining the performance of ChatGPT and other chatbots in dentistry, evaluations of the scientific accuracy, readability, and user satisfaction of their responses to patient questions about head and neck imaging methods remain limited. Providing patients with incorrect or incomplete information about imaging methods and radiation exposure can lead to unnecessary anxiety, false clinical expectations, and negatively impact health decisions. Therefore, evaluating the accuracy of the information provided by AI-powered systems is important. Studies in the literature have evaluated the performance of AI chatbots in various areas of medicine and dentistry. However, there are a limited number of studies on the quality and readability of chatbot responses to patient-focused questions about head and neck imaging methods in dentistry. The aim of this study was evaluate chatbots' responses to questions patients may ask about head and neck imaging methods used in dentistry. In this context, the chatbot responses were analyzed by experts for scientific adequacy, readability, and user satisfaction to assess their potential for patient education and information.

METHODS

Ethical approval was not required for this study because no patient data or personal information was used and the study aimed solely to analyze freely accessible information sources. This study was prepared considering the basic questions that patients might have regarding head and neck imaging methods in dentistry. A set of 20 questions was deemed sufficient to represent the most frequently asked questions by patients regarding head and neck imaging and to enable a comprehensive evaluation of AI chatbot responses. The questions were selected by examining the "Frequently Asked Questions" and "People Also Ask" sections on Google; content from patient information platforms was also used. The selected questions were chosen by consensus by two expert dentists based on the current literature, 'White and Pharoah's Oral Radiology: Principles and Interpretation', and their clinical significance. The questions were posed to ChatGPT-4.5 and Microsoft Copilot in March 2026. All questions were posed to both chatbots in the same sessions, in incognito mode, using identical wording, and in English. No additional guidance were provided during the response generation process, and each question was evaluated independently. The responses were recorded in plain text format by a third evaluator. During the evaluation process, evaluators were not informed which AI model the responses belonged to. Chatbot responses were independently evaluated by two expert evaluators. The scientific accuracy and quality of the responses were assessed using 'White and Pharoah's Oral radiology: Principles and Interpretation', a reference source in the field of oral and maxillofacial radiology (**Table 1**).

Table 1. Patient questions regarding head and neck imaging methods are directed to chatbots

1. In dentistry and medicine, in what situations is tomography (CBCT/CT) preferred, and what kind of information does it provide?
2. In what situations is MRI necessary in dentistry?
3. Is MRI safe in patients with dental implants?
4. In what clinical situations is ultrasonography used in dentistry?
5. What are the main differences between ultrasonography and MRI?
6. What are the differences between CBCT and CT?
7. Are patients exposed to radiation during ultrasonography and MRI imaging?
8. What precautions are taken to protect patients from radiation during radiological imaging?
9. What level of radiation are patients exposed to during tomography (CBCT/CT) scans in dentistry and medicine?
10. Is tomography (especially CBCT) necessary before dental implant planning?
11. How many times can a patient have a CT scan in a year, and what factors determine this decision?
12. Are there any special precautions patients should take after radiographic imaging?
13. Do metal materials in the body affect image quality during a CT scan (CBCT/CT)?
14. Is MRI or CT more suitable for evaluating TMJ problems?
15. Can all diseases be definitively diagnosed with CT/CBCT in medicine and dentistry?
16. Which methods can be safely used for head and neck imaging during pregnancy?
17. What are the differences in cost and accessibility between CBCT, CT, MRI, and ultrasound methods?
18. What risks does the incorrect or unnecessary use of imaging methods pose to patients?
19. What factors do clinicians consider when choosing the appropriate imaging method for a patient?
20. What are the differences between different imaging methods (CBCT, CT, MRI, ultrasound) in terms of scanning times and patient comfort?

CBCT: Cone-beam computed tomography, CT: Computed tomography, MRI: Magnetic resonance imaging, TMJ: Temporomandibular joint

Each response was evaluated using a single overall score on a 7-point Likert scale (1=very poor, 7=excellent), assessing both scientific accuracy and comprehensibility. The readability of responses was assessed using the Flesch Readability Ease Score (FRES) and the Flesch-Kincaid Grade Level (FKGL) indices. Scientific accuracy and the quality of information in the responses were assessed using a 7-point Likert scale, aligned with assessment approaches used in similar studies. On the scale, 1 point was defined as 'very poor (incorrect and potentially harmful)', 2 points as 'poor (contains serious errors and misinformation)', 3 points as 'poor (contains significant omissions and some errors)', 4 points as 'medium (partially correct but contains significant omissions)', 5 points as 'good (contains minor errors or limited omissions)', 6 points as 'very good (almost error-free and contains very minor omissions)', and 7 points as 'excellent (completely accurate, complete, and reliable)'. The data collected in the study were statistically analyzed using IBM SPSS 29.0 software. Skewness and kurtosis values for the FRES, FKGL, and expert scoring variables ranged from -2 to +2; histograms showed a normal distribution (George & Mallery, 2010). Cohen's Kappa was calculated to assess the level of agreement among expert scores. An independent-samples t-test was used to compare index scores and expert-evaluation variables between ChatGPT and Microsoft Copilot. The significance level was set at $p<0.05$ for all statistical analyses.

RESULTS

Inter-Expert Agreement

Cohen's kappa was used to assess the agreement between the two experts' evaluations of the AI responses. As shown in **Table 2**, Cohen's kappa analysis indicated weak (McHugh, 2012) but statistically significant agreement between the scoring styles for AI responses evaluated by the experts (κ=0.399, p<0.001).

Table 2. Cohen's kappa analysis table of agreement between how two experts categorize AI responses

		Expert 2				
		Score 5	Score 6	Score 7	Kappa (κ)	p
Expert 1	Score 5	3	4	0	0.399	<0.001
	Score 6	3	14	5		
	Score 7	3	0	8		

AI: Artificial Intelligence

Chatbot Comparisons

Independent-samples t-tests were conducted to examine whether there was a significant difference between ChatGPT and Microsoft Copilot in FRES, FKGL, and expert scoring. The expert score was created by averaging the two experts' scores. According to the results, there was no significant difference between ChatGPT and Microsoft Copilot in FRES (p=0.815) or expert scoring (p=0.793). On the other hand, Microsoft Copilot's scores were found to be statistically significantly higher than ChatGPT's FKGL scores (p=0.025) (**Table 3**).

Table 3. Independent samples t-test table for comparing various index values between ChatGPT and Copilot

	ChatGPT	Copilot			
	Mean±SD	Mean±SD	t	p	Cohen's d
FRES	32.40±14.39	31.35±13.79	0.236	0.815	0.075
FKGL	10.05±2.04	11.55±2.01	-2.342	0.025	-0.741
Mean expert rating	6.13±0.60	6.08±0.59	0.265	0.793	0.084

SD: Standard deviation, FRES: Flesch Reading Ease Score, FKGL: Flesch–Kincaid Grade Level

DISCUSSION

The main findings of the present study showed that the responses of ChatGPT and Microsoft Copilot to questions regarding head and neck imaging methods in dentistry were similar in terms of scientific quality and user satisfaction. A statistically significant but weak level of agreement was found between expert evaluations. Furthermore, while no significant difference was found between the two chatbots in FRES and expert readability scores, FKGL scores were significantly higher for Copilot. This suggests that Microsoft Copilot's responses may have a more complex language structure. The low level of agreement observed among experts indicates that the evaluation of AI-generated health information is somewhat subjective. This finding may be influenced by the evaluators' clinical experience. However, the differences in scores between evaluators were mostly at the one-point level and did not indicate a significant divergence of opinion in clinical evaluations regarding the overall quality of the responses. Therefore, the low Cohen's kappa coefficient should not be interpreted as indicating a clinically significant discrepancy between evaluations. Similarly, previous studies have reported that chatbot responses can receive different scores depending on experts' experience and evaluation criteria.

Deep learning models have been increasingly used in natural language processing and computer vision. For this purpose, pre-trained LLMs such as ChatGPT and Microsoft Copilot have demonstrated capabilities in text generation and comprehension. The rate of online access to medical and health information is high, and chatbots are frequently used for this purpose.[7] With the development of chatbots, it is possible for patients and healthcare professionals to use these resources to learn about the benefits and risks of different diseases and imaging techniques.[8] However, the ability of AI systems to generate inaccurate, incomplete, or outdated information remains a significant concern for patient safety. A comprehensive evaluation of chatbots' performance in providing accurate and safe information is critical to determining the benefits of these technologies for clinical decision-making and patient education.[9] In recent years, magnetic resonance imaging (MRI), a non-invasive method that does not involve ionizing radiation, has gained prominence in dentistry for imaging soft tissues in the head and neck region, thanks to technical advancements and the development of new sequences. However, its use in dentistry is limited by constraints such as cost, accessibility, and artifact generation.[10,11] The present study also evaluated imaging methods that do not involve ionizing radiation, such as MRI. Providing accurate patient information about the advantages and limitations of MRI, which has seen increased use in the head and neck region in recent years, is crucial. Therefore, it is important to determine whether AI-based systems can provide reliable information about imaging methods that are gaining new applications, such as MRI. In their study, Zhang et al.[7] posed ultrasound-related questions in English and Chinese to the ChatGPT and ERNIE Bot chatbots and evaluated how responses varied by model, language, and question type. They reported that the ERNIE Bot generally performed better than ChatGPT, although both models experienced a lower performance on English questions. Furthermore, they emphasized that while the chatbots were successful in providing basic information, they were more limited in providing diagnostic interpretations. Zhang et al.[7] reported that chatbot performance can vary depending on language and question type. In the present study, although all questions were in English, no significant difference was found between ChatGPT and Microsoft Copilot in terms of overall quality scores. This suggests that the model's performance may converge toward patient-focused, informative questions about imaging methods. In their study, Patil et al.[8] evaluated AI chatbots' responses to scenarios involving imaging modalities such as CT and MRI, considering risks, benefits, alternative imaging options, and the potential consequences of not using contrast agents. ChatGPT has been reported to provide more accurate responses than Google Bard. However, it was emphasized that both models can provide incomplete or misleading information in critical situations and are limited in terms of clinical decision-making. However, in

the present study, ChatGPT and Microsoft Copilot showed similar performance. Furthermore, differences in results across studies conducted at different times may be due to the ongoing updates of AI models. In a study by Mohammad-Rahimi et al.[9] on chatbots, controversial topics in the literature and frequently encountered questions requiring expert knowledge in clinical practice in oral, dental, and maxillofacial radiology were used. The responses from 6 different chatbots were evaluated for quality by expert radiologists, and GPT-4 was reported to perform best. However, the study noted that some of the references provided by the chatbots were unverified. Similar to the present study, this research evaluated the performance of chatbots in patient education and information using frequently asked questions about head and neck imaging methods. The questions used in the present study focused on imaging methods and radiation safety issues that patients frequently wonder about in daily clinical practice. In this regard, the study contributes to the evaluation of chatbots from a patient education perspective.

In this study, the higher FKGL scores found in Copilot indicate that this model tends to use longer sentences and more complex word structures. A high FKGL score suggests that a higher educational level is required to understand the text. However, the lack of a significant difference between the two chatbots in FRES scores suggests that both models exhibit similar reading ease. When evaluated in terms of patient education, lower FKGL values may contribute to easier understanding of information by a wider patient population. The findings show that ChatGPT and Microsoft Copilot can serve as supportive tools for informing patients about head and neck imaging methods, but the information provided by these systems should be verified by healthcare professionals. Future healthcare-focused AI applications should prioritize not only information accuracy but also readability and user-friendly content creation.

Limitations

This study has some limitations. The evaluation was performed using only the ChatGPT and Microsoft Copilot versions available in March 2026. Since AI models are constantly updated, findings may vary across different versions. Furthermore, the study included a limited number of patient questions related to head and neck imaging techniques. Using a broader set of questions might lead to different results. Future studies should include a wider and more diverse set of patient questions, evaluate additional AI chatbots, and assess chatbot performance in different languages and clinical scenarios to contribute to a more comprehensive evaluation of the models' strengths and weaknesses in terms of patient education.

CONCLUSION

In this study, the responses of ChatGPT and Microsoft Copilot to frequently asked patient questions about head and neck imaging techniques were evaluated in terms of scientific accuracy and readability. The findings showed that, according to expert assessments, both chatbots provided similar levels of scientific accuracy and response quality. No significant difference was found between the two models in terms of FRES scores. However, Microsoft Copilot produced significantly higher FKGL scores than ChatGPT, indicating that its responses were linguistically more complex and required a higher educational level for comprehension. Both AI chatbots produced responses that could help inform patients about head and neck imaging techniques. The findings suggest that AI-based chatbots can support patient education and facilitate access to information, but should only serve as complementary tools in clinical decision-making processes under the guidance of healthcare professionals. It should be kept in mind that information from AI may contain errors or omissions and should be verified by healthcare professionals.

ETHICAL DECLARATIONS

Ethics Committee Approval

Ethical approval was not required for this study because no patient data or personal information was used and the study aimed solely to analyze freely accessible information sources.

Informed Consent

This study did not involve human participants, clinical samples, or personal health data; it analyzed only freely available information sources. Therefore, informed consent is not required.

Peer Review Process

This manuscript was subject to external peer review.

Conflict of Interest

The authors declare no conflicts of interest related to this study.

Financial Disclosure

The authors received no financial support for the conduct or publication of this research.

Author Contributions

Conceptualization: MH, AC; Methodology: MH, AC; Software: MH; Validation: MH, AC; Formal Analysis: MH; Investigation: MH; Resources: MH; Data Curation: MH, AC; Writing-Original Draft Preparation: MH; Writing-Review and Editing: MH, AC; Visualization: MH; Supervision: AC; Project Administration: MH.

REFERENCES

1. Guler R, Yalcin E. Performance of AI chatbots in preliminary diagnosis of maxillofacial pathologies. *Med Sci Monit*. 2025;31:e949076. doi:10.12659/MSM.949076
2. Thirunavukarasu AJ, Ting DSJ, Elangovan K, Gutierrez L, Tan TF, Ting DSW. Large language models in medicine. *Nat Med*. 2023;29(8):1930-1940. doi:10.1038/s41591-023-02448-8
3. Çetin P, Onan A. Büyük dil modellerinin tıp eğitimde soru yanıtlama sistemlerinde kullanımı: potansiyel, zorluklar ve gelecek yönelimleri. *JISMCE*. 2025;1(1):82-108.
4. Rokhshad R, Zhang P, Mohammad-Rahimi H, Pitchika V, Entezari N, Schwendicke F. Accuracy and consistency of chatbots versus clinicians for answering pediatric dentistry questions: a pilot study. *J Dent*. 2024;144:104938. doi:10.1016/j.jdent.2024.104938
5. Tan S, Xin X, Wu D. ChatGPT in medicine: prospects and challenges: a review article. *Int J Surg*. 2024;110(6):3701-3706. doi:10.1097/JS9.0000000000001312
6. Jeong H, Han SS, Yu Y, Kim S, Jeon KJ. How well do large language model-based chatbots perform in oral and maxillofacial radiology? *Dentomaxillofac Radiol*. 2024;53(6):390-395. doi:10.1093/dmfr/twae021

7. Zhang Y, Lu X, Luo Y, Zhu Y, Ling W. Performance of Artificial Intelligence chatbots on ultrasound examinations: cross-sectional comparative analysis. *JMIR Med Inform*. 2025;13:e63924. doi:10.2196/63924
8. Patil NS, Huang RS, Caterine S, et al. Artificial Intelligence chatbots' understanding of the risks and benefits of computed tomography and magnetic resonance imaging scenarios. *Can Assoc Radiol J*. 2024;75(3): 518-524. doi:10.1177/08465371231220561
9. Mohammad-Rahimi H, Khoury ZH, Alamdari MI, et al. Performance of AI chatbots on controversial topics in oral medicine, pathology, and radiology. *Oral Surg Oral Med Oral Pathol Oral Radiol*. 2024;137(5):508-514. doi:10.1016/j.oooo.2024.01.015
10. Reda R, Zanza A, Mazzoni A, Cicconetti A, Testarelli L, Di Nardo D. An update of the possible applications of magnetic resonance imaging (MRI) in dentistry: a literature review. *J Imaging*. 2021;7(5):75. doi:10.3390/jimaging7050075
11. Al-Haj Husain A, Zollinger M, Stadlinger B, et al. Magnetic resonance imaging in dental implant surgery: a systematic review. *Int J Implant Dent*. 2024;10(1):14. doi:10.1186/s40729-024-00532-3

Journal of Radiology Medicine in

Original Article

Doi: 10.51271/JRM-0052

Reclassification of inner ear malformations according to the updated Sennaroğlu classification: which categories change?

Melih Akşamoğlu*, Ahmet Selim Kervancıoğlu

Department of Radiology, Faculty of Medicine, Gaziantep University, Gaziantep, Turkiye

Received: 12.08.2026 ◆ **Accepted**: 15.09.2026 ◆ **Published**: 19.09.2026

Cite this article: Akşamoğlu M, Kervancıoğlu AS. Reclassification of inner ear malformations according to the updated Sennaroğlu classification: which categories change? *J Radiol Med*. 2026;3(3):59-65. doi:10.51271/JRM-0052

***Corresponding Author:** Melih Akşamoğlu, draksamoglu@gmail.com

ABSTRACT

Aims: To determine how many ears change category, and which categories are affected, when a cochlear implant (CI) candidate cohort classified in 2009 is reassessed according to the up-to-date Sennaroğlu classification.

Methods: Preoperative temporal bone computed tomography studies of 100 consecutive CI candidates (200 ears) examined between 2006 and 2008 were re-evaluated, and the measurements repeated, by the radiologist who had made the original assessment, with the earlier category concealed. Ears were re-categorized according to Sennaroğlu's current 2017 classification.

Results: A congenital cochlear malformation was present in 38 ears (19.0%) of 20 patients. Of the 200 ears, 176 (88.0%) kept a category with a direct equivalent in the 2017 scheme, 12 were subtyped within cochlear hypoplasia (CH) and 2 remained unclassifiable because of labyrinthine ossification; no ear was reassigned to a different entity. Ten ears with an isolated abnormality of the vestibule or the semicircular canals could not be categorized under the 2017 scheme. A subdivision of CH applied locally in 2009 mapped onto the current subtypes without crossover. At a threshold of 3.0 mm, all 8 ears with a narrow internal auditory canal in the coronal plane had a malformed cochlea; the axial plane performed less consistently at every threshold tested.

Conclusion: Following reclassification based on current criteria, redistribution was limited to cochlear hypoplasia, but ten ears were left without a category. Because the boundaries between some cochlear malformations are defined descriptively rather than numerically, their applicability may be limited.

Keywords: Cochlea, temporal bone, cochlear implantation, computed tomography, sensorineural hearing loss

INTRODUCTION

Congenital sensorineural hearing loss (SNHL) is most often caused by membranous malformations that leave the bony labyrinth intact and cannot be demonstrated radiologically. In the remaining fifth of cases the bony labyrinth is involved, and these malformations can be shown by computed tomography (CT) and magnetic resonance imaging.[1] Because this group presents both surgical difficulties and problems in decision making, its preoperative recognition is a routine part of the assessment of cochlear implant (CI) candidates.[1]

The category is not merely descriptive: it guides electrode choice, signals the risk of cerebrospinal fluid gusher and facial nerve injury, and bears on the choice between cochlear and auditory brainstem implantation and on the expected outcome.[1,2] A change in category is therefore a change in clinical meaning.

Classification schemes have evolved over time: Jackler et al.[3] first grouped these malformations by the stage of arrested embryogenesis, Sennaroğlu and Saatci[4] later divided incomplete partition (IP) into types I and II (IP-I and IP-II),[4] and the scheme was revised in 2010 and again in 2017.[1,5] In the earlier version, cochlear malformations were classified into six groups, while the vestibule, the semicircular canals (SCCs), the internal auditory canal (IAC) and the aqueducts were assessed on separate axes.[4] The current version brings all of these under a single heading of inner ear malformations, in eight categories, and adds subgroups such as IP type III (IP-III) and four subtypes of cochlear hypoplasia (CH), designated CH-I to CH-IV. Cochlear aperture (CA) abnormalities are included as a category of their own.[1] Other schemes have been proposed, but the Sennaroğlu classification remains the most widely accepted.[6-8]

These revisions have a consequence that is rarely addressed directly. A large body of work published before 2017, including prevalence figures, surgical series, and audiological correlations, was categorized under earlier schemes. If the boundaries between categories have moved, the comparability of that work with contemporary reports cannot simply be assumed. To our knowledge, the extent to which a cohort classified under the earlier scheme is redistributed when the current criteria are applied has not been quantified.

We therefore reexamined the preoperative temporal bone CT studies of a CI candidate cohort that had been classified in 2009, applying the 2017 criteria, in order to determine how many ears change category and which categories are affected.

METHODS

Ethics

This study was approved by the Gaziantep University Medical Ethics Committee of the Faculty of Medicine, (Date: 19.02.2009, Decision No: 02-2009/20). All procedures were carried out in accordance with the ethical rules and the principles of the Declaration of Helsinki.

Study Design and Patients

This retrospective study was carried out at a tertiary referral center. Consecutive patients assessed by the department of otorhinolaryngology, referred as CI candidates and examined by temporal bone CT in our department between January 2006 and December 2008 were included. All had bilateral severe to profound SNHL. Patients were excluded if their imaging could not be retrieved from the archive or if the CT had been performed at another institution. Examinations degraded by motion were repeated at the time, so no study was excluded on grounds of image quality. Ears with acquired pathology were retained, and the acquired finding was recorded separately from the congenital category. The final cohort comprised 100 patients (200 ears), 52 male and 48 female, aged 1 to 36 years (mean 4.9; median 3.0). Ninety-six patients were younger than 18 years. Adults were retained because the unit of analysis is the ear rather than the patient.

The cohort and its original radiological assessment were reported in an academic thesis in 2009.[9] The present study reanalyzes the same imaging material under a different classification system, using the original findings only as the comparator; the reclassification reported here has not been published previously.

Imaging Technique

CT was performed on a six-detector-row scanner (Brilliance CT; Philips Medical Systems, Best, The Netherlands), with sedation where required. The temporal bones were scanned continuously in the axial plane at 120 kV and 250 mAs, and images were reconstructed with a bone algorithm at 0.8 mm section thickness.

To allow consistent comparison between sides, axial reformats were generated with both inner ears at the same level and with the anterior and posterior limbs of the lateral SCC visible in a single section. Coronal reformats were then obtained perpendicular to this plane, at 0.8 mm section thickness. Images were reviewed at a window width of 4095 and a window level of 600.

Image Analysis

For the present study all CT examinations were re-evaluated and all measurements were repeated by a single radiologist with 17 years of experience in temporal bone imaging, who had also performed the original assessment in 2009. The earlier category was concealed until the new category had been recorded.

Classification

Ears were classified according to the eight categories of Sennaroğlu and Bajin.[1] Acquired pathology was recorded separately from the congenital category, so that an ear could carry both.

In ears with labyrinthine ossification, a congenital category was assigned when cochlear morphology, that is the number of turns and the presence of the modiolus and the interscalar septa, remained assessable; when ossification obscured these structures the ear was recorded as unclassifiable.

We drew the boundary between CH-II and IP-I at a cochlear height of 4.4 mm, the lower limit of the normal range reported in a normative series;[10] this threshold was adopted for the present study.

Measurements

The CA,[11,12] the cochlear height[10,13] and the IAC[1,14] were measured as previously described and as illustrated in **Figure 1**. Reported thresholds differ. For the CA we used 1.5 mm, as in recent reports from the group that proposed the classification,[11,12] rather than the 1.4 mm stated in the classification itself;[1] a CA was recorded as aplastic when no bony cochlear nerve canal could be identified. For cochlear height we used the operational threshold of 4.4 mm described above,[10] a value that does not require adjustment for age.[13] For the IAC, criteria differ in both the value and the site of measurement, so four values were applied in both planes as a sensitivity analysis rather than as validated criteria for either plane: 2.0 mm,[15] 2.5 mm,[1] 3.0 mm[9] and 3.2 mm.[14] Because the CA measurement alone determines a category, it was obtained twice in separate sessions and the mean of the two values was used.

The vestibular aqueduct (VA) was considered enlarged when it appeared wider than the neighboring posterior SCC on an axial section displaying both.[14] Ears in which the aqueduct was not visualized were recorded separately and analyzed as not enlarged.

The vestibule, the SCCs and the ossicular chain were assessed qualitatively.

Comparison Between Classifications

The scheme used in the original assessment comprised six categories of cochlear malformation: Michel deformity, cochlear aplasia, common cavity (CC), CH, IP-I and IP-II.[4,9] Categories were treated as concordant when the earlier label had a direct equivalent in the current system; ears originally

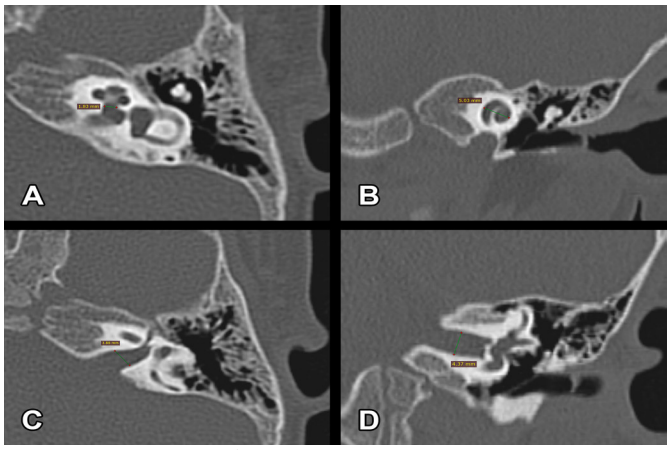

Figure 1. Measurement techniques

(A) Cochlear aperture, measured in the axial plane at the mid-modiolar level from the inner margins of its bony walls. (B) Cochlear height, measured in the coronal plane on the section of greatest height showing both the basal and the apical turn, between the centers of these two turns. (C) Internal auditory canal, measured at its midpoint in the axial plane. (D) Internal auditory canal, measured at its midpoint in the coronal plane.

assigned to CH, a single group at that time, were recorded as subtyped rather than changed.

The original assessment had also used a local subdivision of CH according to the degree of development of the internal architecture, and separate local categories for an isolated hypoplastic vestibule and for isolated dysplastic SCCs.[9] None of these is part of a published classification, and they are reported here as secondary observations.

Statistical Analysis

Categorical data are reported as counts and percentages, and continuous data as mean with standard deviation and range. Agreement between the two CA measurements was assessed with the intraclass correlation coefficient (ICC; two-way random effects, absolute agreement, single measures) and the Bland-Altman method, excluding ears in which no canal could be identified. Because both ears of every patient were included, ear-level proportions are reported descriptively. Analyses were performed with SPSS Statistics 20.0 (IBM Corp., Armonk, NY, USA).

RESULTS

Cohort

A congenital cochlear malformation was present in 38 ears of 20 patients (19.0% of ears, 20.0% of patients). Acquired pathology was recorded in 9 ears: labyrinthitis ossificans in 7 and otosclerosis in 2.

Redistribution Between the Two Classifications

Of the 200 ears, 176 (88.0%) kept a category with a direct equivalent in the 2017 scheme, and no ear was reassigned to a different entity (**Table 1**).[9] The 12 ears grouped as CH in the earlier scheme were distributed across all four current subtypes: CH-I in 1 ear, CH-II in 1, CH-III in 8 and CH-IV in 2 (**Figure 2**). Two ears remained unclassifiable because labyrinthine ossification obscured cochlear morphology.

Ten further ears had been recorded as normal under the earlier scheme, which classified cochlear malformations, but have no category in the current one, which covers inner ear malformations: each had an isolated abnormality of the vestibule or the SCCs.

None of the entities added in the 2017 revision was identified in this cohort. There were no ears with rudimentary otocyst, IP-III, isolated enlarged VA or isolated CA abnormality. Every ear with an abnormal CA also had a cochlear malformation that had already been recognized in the original assessment.[9]

Table 1. The 200 ears distributed under the 2002 and the 2017 classifications, with the local subdivision used in 2009 and the modifications suggested here

	2002 scheme		2009 local subdivision			2017 scheme			Suggested modification		
	Category	n	Category	n		Category	Subgroup	n	Category	Subgroup	n
Cochlear malformations	MD		MD		Inner ear malformations	MD	3 subgroups		MD	3 subgroups	
	Not in scheme					RO	-		RO	-	
	CAp		CAp			CAp	2 subgroups		CAp	2 subgroups	
	CC	1	CC	1		CC	-	1	CC	-	1
	CH	12	Type 1	2		CH	CH-I	1	CH	CH-I	1
							CH-II	1		CH-II	1
			Type 2	10			CH-III	8		CH-III	8
							CH-IV	2		CH-IV	2
	IP-I	11	IP-I	11			IP-I	11		IP-I	11
	IP-II	12	IP-II	12		IP	IP-II	12	IP	IP-II	12
	Not in scheme						IP-III			IP-III	
	Categorized under another heading					EVA	-		IEVA*	-	
	Not in scheme					CAA	-		ICAA*	-	
	Categorized under another heading					No category		10	IVSA**	-	10
	Normal	162	Normal	162		Normal		152	Normal		152
	Unclassifiable	2	Unclassifiable	2		Unclassifiable		2	Unclassifiable		2
	Total	200	Total	200		Total		200	Total		200

Category gives the name of the category in each scheme, and Subgroup the subgroup where a scheme subdivides it; n is the number of ears assigned. Blank cells indicate that no ear was assigned, and a dash that the scheme defines no subgroup. "Not in scheme" indicates a category that did not exist at that time, "categorized under another heading" a structure assessed in 2002 outside the list of cochlear categories, and "no category" ears for which the 2017 scheme provides none. Italics indicate entries that are not part of the corresponding published scheme; * denotes a suggested change of name and ** a suggested new category. n: Number of ears, MD: Michel deformity, RO: Rudimentary otocyst, CAp: Cochlear aplasia, CAA: Cochlear aperture abnormalities, CC: Common cavity, CH: Cochlear hypoplasia, CH-I to CH-IV: Cochlear hypoplasia types I to IV, EVA: Enlarged vestibular aqueduct, ICAA: Isolated cochlear aperture abnormalities, IEVA: Isolated enlarged vestibular aqueduct, IP: Incomplete partition, IP-I to IP-III: Incomplete partition types I to III, IVSA: Isolated vestibular and/or semicircular canal abnormality

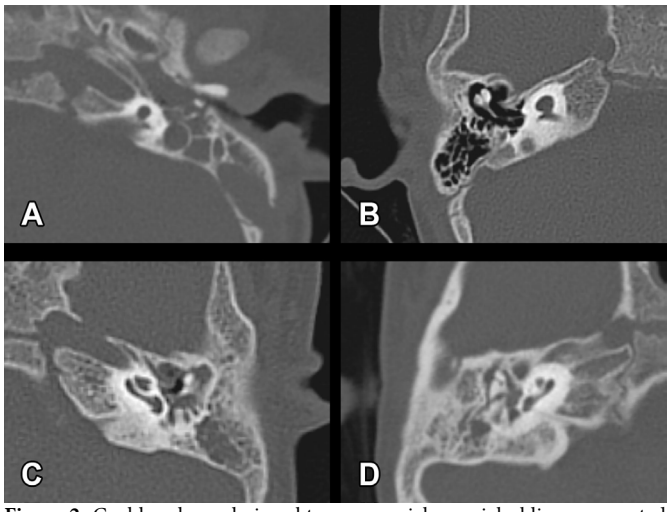

Figure 2. Cochlear hypoplasia subtypes on axial or axial-oblique computed tomography, one ear of each subtype

(A) CH-I, a bud-like cochlea in which no internal architecture can be recognized. (B) CH-II, a small cochlea with defective internal architecture; the ossicles within the field of view are also dysplastic. (C) CH-III, a proportionally small cochlea. (D) CH-IV, a normal basal turn with hypoplastic middle and apical turns. CH-I to CH-IV: Cochlear hypoplasia types I to IV

Local Subdivision of Cochlear Hypoplasia

In the 2009 assessment the hypoplastic ears had been divided locally into those in which the internal architecture was absent (type 1) and those in which it was partially developed (type 2).[9] This subdivision mapped onto the current subtypes without overlap (**Table 1**). Both type 1 ears became CH-I or CH-II, and all 10 type 2 ears became CH-III or CH-IV. No ear crossed between the two pairs.

Cochlear Aperture

The CA could be measured in 198 ears. In the remaining 2 ears, both belonging to the same patient, no bony cochlear nerve canal could be identified and the CA was recorded as aplastic. The mean of the two measurements was 1.94 mm (SD 0.22, range 0.83 to 2.60). Agreement between them was good, with an ICC of 0.87, a mean difference of -0.01 mm and 95% limits of agreement of -0.24 to 0.22 mm.

In 5 ears (2.5%) the CA measured below 1.5 mm and was classified as hypoplastic. Together with the 2 aplastic apertures, 7 ears met the current criteria for a CA abnormality. These were the same 7 ears in which a narrow CA had been reported in the original assessment.[9] All 7 belonged to patients in whom a cochlear malformation had already been recognized.

Cochlear Height

Cochlear height could be measured in 197 ears. It was not measurable in 2 ossified ears and in 1 ear with a CC. The mean was 4.96 mm (SD 0.45, range 2.90 to 6.00). Twelve ears fell below 4.4 mm, and all 12 belonged to the CH group identified in the original assessment.[9]

Internal Auditory Canal

The mean mid-portion width was 4.48 mm (SD 0.92, range 2.10 to 8.80) in the axial plane and 4.69 mm (SD 1.04, range 1.50 to 8.80) in the coronal plane.

The two planes did not identify the same ears (**Table 2**). In the coronal plane, every ear that measured below 3.0 mm had a malformed cochlea, and only at 3.2 mm did 2 of the 11 ears identified have a normal one. In the axial plane, fewer malformed ears were identified at every threshold, and ears with a normal cochlea appeared earlier and in greater number. At 3.0 mm, 8 ears were narrow in the coronal plane and 7 in the axial plane, but only 4 were narrow in both. In one patient with bilateral IP-I the canal exceeded 3.0 mm in the axial plane on both sides but was narrow in the coronal plane (**Figure 3**).

Table 2. Ears identified as having a narrow internal auditory canal at four thresholds, in each plane

Threshold	Coronal plane narrow IAC (malf; norm)	Axial plane narrow IAC (malf; norm)	Both planes narrow IAC (malf; norm)
2.0 mm	1 (1; 0)	0 (0; 0)	0 (0; 0)
2.5 mm	6 (6; 0)	2 (2; 0)	1 (1; 0)
3.0 mm	8 (8; 0)	7 (4; 3)	4 (4; 0)
3.2 mm	11 (9; 2)	11 (4; 7)	4 (4; 0)

Values in parentheses give the number of ears with and without a cochlear malformation. Measurements were made at the mid-portion of the canal in the axial and coronal plane. The thresholds are the most widely used criterion (2.0 mm), the value stated in the 2017 classification (2.5 mm), the criterion of the original assessment (3.0 mm), and two standard deviations below the normative coronal mid-portion mean (3.2 mm). None of the ears listed had acquired pathology, and every ear counted as having a normal cochlea also had a normal vestibule and normal semicircular canals. IAC: Internal auditory canal, malf, ears with a cochlear malformation, norm, ears with a normal cochlea

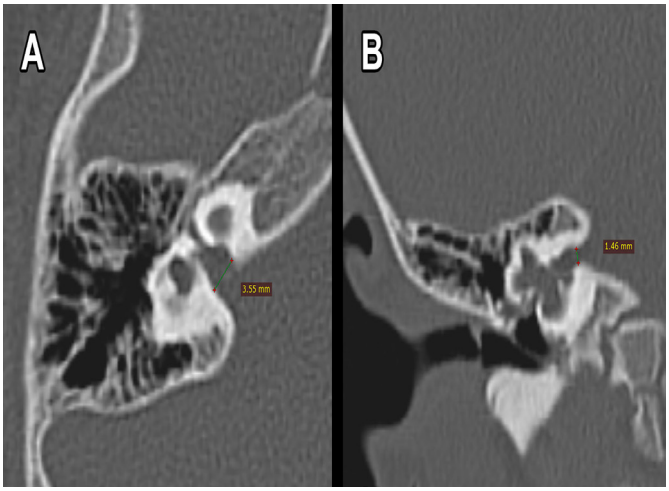

Figure 3. Internal auditory canal in the right ear of a patient with bilateral incomplete partition type I

In the axial plane (A) the canal appears unremarkable, whereas in the coronal plane (B) the same canal is narrow. Measurement confined to the axial plane would not have identified this canal as narrow

Accompanying Findings

The vestibule was normal in 166 ears, dilated in 15, hypoplastic in 14 and absent in 2, and formed part of a CC in 1 ear. In 1 ear it was considered probably normal despite partial ossification, and in 1 ear ossification prevented assessment. The SCCs were normal in 165 ears, dysplastic in 26 and aplastic in 2; 3 ears were considered probably normal despite partial ossification, and in 4 ears ossification prevented assessment. The VA was enlarged in 15 ears of 9 patients, all of which had a malformed cochlea (IP-II in 12 and IP-I in 3), and was not visualized in 5 ears.

Ten ears in 5 patients had an isolated abnormality of the vestibule or of the SCCs with a normal cochlea: A hypoplastic vestibule in 4 ears and dysplastic SCCs in 6.

Ossicular chain malformation was present in 9 ears of 5 patients, 7 of them in ears with a cochlear malformation.

DISCUSSION

Applying the 2017 criteria to our cohort left most ears where they had been. Eighty-eight percent retained a category with a direct equivalent and no ear was reassigned to a different entity; the only redistribution occurred within CH, which is a single group in the earlier scheme and four subtypes in the current one. Ten ears, however, were left without any category at all.

The redistribution itself could have practical implications for reading the older literature. Prevalence figures and surgical series published before 2017 appear to remain broadly comparable with contemporary reports, at least for the categories represented in this cohort. The exception is CH. In the earlier scheme it was one category; it is now four, and these four have been reported to differ in hearing level.[16] A prevalence figure for CH published before 2017 therefore covers a mixed group and cannot be read as equivalent to a figure for any one of the current subtypes.

The way the hypoplastic ears redistributed is worth noting. The 2009 assessment had divided them locally according to whether the internal architecture could be recognized,[9] and this division mapped onto the current subtypes without a single crossover. Both schemes separated the same ears on the same feature, namely whether the modiolus and the interscalar septa can be identified. The finding is limited by the small number of ears and by the fact that the same observer made both assessments, but it does suggest that this feature is a natural dividing line and can be applied consistently.

None of the categories introduced in the 2017 revision was found in our cohort. Rudimentary otocyst and IP-III are uncommon. In a recent series of 155 malformed ears, rudimentary otocyst accounted for 3.2%, an isolated enlarged VA for 3.9%, and IP-III was likewise not encountered;[8] a cohort containing 38 malformed ears would not be expected to include them. Although no isolated CA abnormality or isolated enlarged VA was newly identified in this cohort, that absence cannot be generalized, since the 2009 protocol had already assessed both structures independently of the state of the cochlea.[9] How far an older report is comparable with a current one may therefore depend as much on how thoroughly the temporal bone was assessed at the time as on which categories were then available.

The 2017 revision also changed the scope of the scheme. The earlier version classified cochlear malformations and assessed the vestibule, the SCCs, the IAC and the aqueducts on separate axes,[4] whereas the current version brings all inner ear structures into a single list of eight categories.[1] Ears with an isolated abnormality of the vestibule or the SCCs, which had a place in the earlier scheme, therefore have none in the current one: by the heading of the classification they are inner ear malformations, yet no category accommodates them. Ten ears in this cohort were of this kind (**Table 1**).

Two of the eight categories are also defined differently from one another. The enlarged VA category requires a normal cochlea, vestibule and SCCs and is thus restricted to the isolated form, although its title does not say so. No such restriction is placed on CA abnormalities, which are explicitly said to occur either with other malformations or with a normal cochlea;[1] an ear with both a cochlear malformation and an abnormal CA therefore has no stated rule for assignment, and all seven such ears in this cohort were of that kind. A recent series classified under the current scheme meets the same difficulty: enlarged VA had to be reported separately as isolated and as associated with other anomalies, and CA abnormality was reported as a finding across the whole cohort rather than as one of the eight categories.[8] A category for isolated vestibular and/or SCC abnormalities, and titles that state whether the isolated form is meant, would remove both difficulties (**Table 1**).

Two boundaries in the current scheme rest on size without a numerical definition. CH-I, CH-II and IP-I all lack the modiolus and the interscalar septa, and are separated by how large the cochlea is; yet the 2017 classification states no measurement for this. We had to adopt a threshold from an independent normative study,[10] derived from normal cochleae rather than malformed ones. A classification whose categories are separated by size would be easier to apply if the measurement were specified within the classification itself. The distinction between CH-III and CH-IV is also made without a numerical criterion. The published definitions, fewer than two turns versus hypoplastic middle and apical turns with a normal basal turn, are not mutually exclusive. In practice the distinction rests on whether the cochlea is proportionally or disproportionately small, with the middle and apical turns affected more than the basal turn. In one morphometric series the basal turn length of the two subtypes fell in a similar range,[17] and although one series found CH-IV to differ clearly from the other three in hearing level,[16] that comparison has not been repeated.

Two further difficulties affect measurement in malformed ears. The axial plane is conventionally aligned with the lateral SCC, but that canal is itself dysplastic in some malformed ears, so neither the axial plane nor the coronal plane derived from it can be standardized. Cochlear height is defined between the centers of the basal and the apical turn, which presupposes that both can be identified; in a cystic cochlea there are no turns and the endpoints become a matter of judgment. The ears in which size determines the category may thus be those in which size is hardest to measure consistently.

An incidental observation concerns the IAC. The coronal and the axial plane did not identify the same ears. At every threshold the coronal plane identified more of the ears with a cochlear malformation than the axial plane did, and it included no ear with a normal cochlea until 3.2 mm. The axial plane identified fewer malformed ears at each threshold and, from 3.0 mm upward, an increasing proportion of the ears it identified had a normal cochlea. In one patient with bilateral IP-I the canal appeared unremarkable in the axial plane and markedly narrow in the coronal plane.

Part of the explanation may lie in where the measurements that underlie the published criteria were taken. Normative data exist for the coronal mid-portion, the site used here: a mean midpoint width of 5.06 mm[14] and a mean maximum height of 4.62 mm[18] have been reported in controls. To our

knowledge, no comparable normative data exist for the axial mid-portion. The axial measurements in the literature were taken at the porus or a short distance inside it,[14,15,18] where the canal is wider, or at its narrowest point.[19] The thresholds themselves are equally varied: below 2.0 mm is the most widely used criterion,[15] the 2017 classification states 2.5 mm at the midpoint without giving a source,[1] and 3.0 mm at the porus has also been used.[20] The width of a normal canal ranges from about 2 to 12 mm, with a mean near 5 mm,[21] and in one series the variation between normal subjects was large enough in the axial plane that no threshold could be derived, whereas one could be derived for coronal measurements.[19] A single number applied without reference to the site of measurement is therefore unlikely to travel well between series.

The reliability of the measurement is a further difficulty. The canal has been described as too variable in shape and course for measurement to be consistent,[14,22] and volumetric assessment is more reliable between raters than diameter, with ICCs of 0.92 and 0.77 respectively.[15] A study that measured the height, width and cross-sectional area of the canal found that none of them distinguished children with cochlear nerve deficiency from controls, whereas the CA did.[23] A single axial diameter may therefore be a weak basis for calling a canal narrow, and the coronal plane should not be omitted.

Limitations

This study has several limitations. The imaging dates from 2006 to 2008 and was acquired on a six-detector-row scanner; although the 0.8 mm reconstructions allowed the modiolus and the interscalar septa to be assessed, the thinner sections available today may allow better assessment of the internal architecture. The present analysis was based on CT alone. Magnetic resonance imaging had been performed in part of the cohort at the time of the original assessment, but cochlear nerve status was not reassessed here, so the categories assigned in this study rest on bony anatomy alone. All readings were made by one radiologist who had also performed the original assessment; although the earlier category was concealed during review, recall could not be excluded, and neither intraobserver nor interobserver reliability could be established for the categorical assessment. The IAC was measured only once, so the reliability of that measurement in this series is unknown, and the comparison between planes should be read with that in mind. Finally, several categories were represented by few ears or by none at all, so the study says nothing about how ears in the unrepresented categories would be redistributed, and the secondary analysis rests on only 12 hypoplastic ears.

CONCLUSION

Reclassification of this cohort under the 2017 criteria changed little. No ear moved to a different entity, and redistribution was confined to CH, where a single group became four subtypes; ten ears, however, were left without a category. Since the boundaries between the cystic cochlear malformations, that is IP-I, CH-I and CH-II, and between CH-III and CH-IV, are defined descriptively rather than numerically, their application rests on observer judgment. The scheme leaves ears with an isolated vestibular and/or SCC abnormality without a category, and defines its enlarged VA and CA categories on different terms; both could be clarified. In this cohort coronal measurement of the IAC identified the affected ears more consistently than axial measurement did, although the number of ears was small.

ETHICAL DECLARATIONS

Ethics Committee Approval

This study was approved by the Gaziantep University Medical Ethics Committee of the Faculty of Medicine, (Date: 19.02.2009, Decision No: 02-2009/20).

Informed Consent

As this was a retrospective study, formal written informed consent was not required and was therefore not obtained. This retrospective study used pre-existing anonymized patient data. No additional intervention was performed, and there was no direct patient contact. The study was approved by the Ethics Committee, and the requirement for written informed consent was waived by the ethics committee.

Peer Review Process

This manuscript was subject to external peer review.

Conflict of Interest

The authors declare no conflicts of interest related to this study.

Financial Disclosure

The authors received no financial support for the conduct or publication of this research.

Author Contributions

Concept: MA, ASK; Design: MA, ASK; Control: ASK; Data Collection and/or Processing: MA; Analysis and/or Interpretation: MA, ASK; Literature Review: MA; Article Writing: MA; Critical Review: MA, ASK.

REFERENCES

1. Sennaroğlu L, Bajin MD. Classification and current management of inner ear malformations. *Balkan Med J.* 2017;34(5):397-411. doi:10.4274/balkanmedj.2017.0367
2. Papsin BC. Cochlear implantation in children with anomalous cochleovestibular anatomy. *Laryngoscope.* 2005;115(1 Pt 2 Suppl 106):1-26. doi:10.1097/00005537-200501001-00001
3. Jackler RK, Luxford WM, House WF. Congenital malformations of the inner ear: a classification based on embryogenesis. *Laryngoscope.* 1987;97(3 Pt 2 Suppl 40):2-14. doi:10.1002/lary.5540971301
4. Sennaroglu L, Saatci I. A new classification for cochleovestibular malformations. *Laryngoscope.* 2002;112(12):2230-2241. doi:10.1097/00005537-200212000-00019
5. Sennaroglu L. Cochlear implantation in inner ear malformations-a review article. *Cochlear Implants Int.* 2010;11(1):4-41. doi:10.1002/cii.416
6. Jeong SW, Kim LS. A new classification of cochleovestibular malformations and implications for predicting speech perception ability after cochlear implantation. *Audiol Neurootol.* 2015;20(2):90-101. doi:10.1159/000365584
7. Adibelli ZH, Isayeva L, Koc AM, Catli T, Adibelli H, Olgun L. The new classification system for inner ear malformations: the INCAV system. *Acta Otolaryngol.* 2017;137(3):246-252. doi:10.1080/00016489.2016.1247498
8. Young YMC, Leung HS, Chang WT, et al. Imaging of inner ear malformation in paediatric patients-a 10-year tertiary centre review. *Eur Radiol.* 2025;35(11):6735-6744. doi:10.1007/s00330-025-11663-5

9. Akşamoğlu M. Assessment of preoperative computed tomography and magnetic resonance imaging in cochlear implant candidates. Medical specialty thesis. Gaziantep University Faculty of Medicine; 2009. Thesis No. 230163.
10. Purcell DD, Fischbein NJ, Patel A, Johnson J, Lalwani AK. Two temporal bone computed tomography measurements increase recognition of malformations and predict sensorineural hearing loss. *Laryngoscope*. 2006;116(8):1439-1446. doi:10.1097/01.mlg.0000229826.96593.13
11. Tahir E, Bajin MD, Atay G, Mocan BÖ, Sennaroğlu L. Bony cochlear nerve canal and internal auditory canal measures predict cochlear nerve status. *J Laryngol Otol*. 2017;131(8):676-683. doi:10.1017/S0022215117001141
12. Miyasaka M, Nosaka S, Morimoto N, Taiji H, Masaki H. CT and MR imaging for pediatric cochlear implantation: emphasis on the relationship between the cochlear nerve canal and the cochlear nerve. *Pediatr Radiol*. 2010;40(9):1509-1516. doi:10.1007/s00247-010-1609-7
13. Mori MC, Chang KW. CT analysis demonstrates that cochlear height does not change with age. *AJNR Am J Neuroradiol*. 2012;33(1):119-123. doi:10.3174/ajnr.A2713
14. Shim HJ, Shin JE, Chung JW, Lee KS. Inner ear anomalies in cochlear implantees: importance of radiologic measurements in the classification. *Otol Neurotol*. 2006;27(6):831-837. doi:10.1097/01.mao.0000227902.47483.ef
15. Bächinger D, Breitsprecher TM, Pscheidl A, et al. Internal auditory canal volume in normal and malformed inner ears. *Eur Arch Otorhinolaryngol*. 2023;280(5):2149-2154. doi:10.1007/s00405-022-07676-1
16. Cinar BC, Batuk MO, Tahir E, Sennaroglu G, Sennaroglu L. Audiologic and radiologic findings in cochlear hypoplasia. *Auris Nasus Larynx*. 2017;44(6):655-663. doi:10.1016/j.anl.2016.12.002
17. Pamuk G, Pamuk AE, Akgöz A, Bajin MD, Özgen B, Sennaroğlu L. Radiological measurement of cochlear dimensions in cochlear hypoplasia and its effect on cochlear implant selection. *J Laryngol Otol*. 2021;135(6):501-507. doi:10.1017/S0022215121000979
18. McClay JE, Tandy R, Grundfast K, et al. Major and minor temporal bone abnormalities in children with and without congenital sensorineural hearing loss. *Arch Otolaryngol Head Neck Surg*. 2002;128(6):664-671. doi:10.1001/archotol.128.6.664
19. Ionescu EC, Reynard P, Idriss SA, Ltaief-Boudriga A, Joly CA, Thai-Van H. The "near"-narrowed internal auditory canal syndrome in adults: clinical aspects, audio-vestibular findings, and radiological criteria for diagnosis. *J Clin Med*. 2023;12(24):7580. doi:10.3390/jcm12247580
20. Masuda S, Usui S, Matsunaga T. High prevalence of inner-ear and/or internal auditory canal malformations in children with unilateral sensorineural hearing loss. *Int J Pediatr Otorhinolaryngol*. 2013;77(2):228-232. doi:10.1016/j.ijporl.2012.11.001
21. Valvassori GE, Garcia Morales F, Palacios E, Dobben GE. MR of the normal and abnormal internal auditory canal. *AJNR Am J Neuroradiol*. 1988;9(1):115-119.
22. Purcell D, Johnson J, Fischbein N, Lalwani AK. Establishment of normative cochlear and vestibular measurements to aid in the diagnosis of inner ear malformations. *Otolaryngol Head Neck Surg*. 2003;128(1):78-87. doi:10.1067/mhn.2003.51
23. Sorge M, Sorge I, Pirlich M, et al. Diameter of the cochlear nerve canal predicts cochlear nerve deficiency in children with sensorineural hearing loss. *Rofo*. 2022;194(10):1132-1139. doi:10.1055/a-1826-0641

Journal of Radiology Medicine in

Original Article

Doi: 10.51271/JRM-0053

Opportunistic screening for the presence of vertebral fractures using L1 trabecular bone density on non-contrast chest CT

Hasan Eryeşil*[1], Abdullah Enes Ataş[2], Hasan Emin Kaya[3]

[1]Department of Radiology, Tatvan State Hospital, Bitlis, Turkiye
[2]Department of Radiology, Faculty of Medicine, Necmettin Erbakan University, Konya, Turkiye
[3]Department of Radiology, Faculty of Medicine, Bursa Uludağ University, Bursa, Turkiye

Received: 12.08.2026 ◆ **Accepted**: 16.09.2026 ◆ **Published**: 19.09.2026

Cite this article: Eryeşil H, Ataş AE, Kaya HE. Opportunistic screening for the presence of vertebral fractures using L1 trabecular bone density on non-contrast chest CT. *J Radiol Med*. 2026;3(3):66-70. doi:10.51271/JRM-0053

***Corresponding Author:** Hasan Eryeşil, hsneryesil@gmail.com

ABSTRACT

Aims: To evaluate the effectiveness of opportunistic screening using L1 trabecular density on non-contrast chest CT for identifying the presence of vertebral fractures.

Methods: This retrospective cross-sectional study included 385 adult patients (≥40 years) who underwent non-contrast chest CT. L1 trabecular attenuation was measured at the mid-vertebral level. Vertebral compression fractures were assessed. The diagnostic performance of L1 hounsfield unit (HU) and clinical variables was evaluated using regression and ROC analyses.

Results: Vertebral fractures were found in 137 patients (35.6%). Mean L1 density was significantly lower in the fracture group (71.2±35.1 HU) compared to the non-fracture group (134.4±36.6 HU, p<0.001). L1 HU showed a strong inverse correlation with age (r=-0.952). ROC analysis for L1 HU yielded an AUC of 0.882. An optimal threshold of 94 HU demonstrated 86.9% sensitivity and 89.1% specificity.

Conclusion: L1 trabecular attenuation on routine non-contrast chest CT serves as a useful opportunistic screening tool associated with the presence of vertebral fractures.

Keywords: Osteoporosis, osteoporotic fractures, computed tomography, mass screening, bone density

INTRODUCTION

With the aging global population, osteoporosis and associated fragility fractures have become a universal public health problem, resulting in significant morbidity, mortality, and a substantial burden on healthcare economics.[1] To frame this clinical challenge, it is important to clearly distinguish between the underlying pathology and its clinical manifestations: osteoporosis is a systemic skeletal disorder characterized by microarchitectural deterioration; bone mineral density (BMD) is the primary quantitative metric used to diagnose this underlying condition; and vertebral compression fractures (VCF) represent the most common, critical clinical consequence of this compromised bone strength. Although these fractures dramatically reduce patients' quality of life and are associated with an increased risk of death, they are often underdiagnosed in clinical practice due to their asymptomatic or subtle presentation, thereby missing opportunities for treatment.[2] In current clinical guidelines, the gold standard method for assessing fracture risk and diagnosing osteoporosis is the calculation of BMD using dual-energy X-ray absorptiometry (DXA). However, limited community-based access to DXA scans, low compliance with screening protocols, and conditions such as aortic vascular calcifications, osteophytes, or degenerative joint diseases which can artificially elevate BMD values, limit the diagnostic accuracy of this method in certain situations.[3]

The concept of "opportunistic screening," which has gained increasing acceptance in the field of radiology in recent years, essentially involves using existing computed tomography (CT) images obtained for a different clinical indication (e.g., lung cancer screening,[4] suspected pneumonia, cardiovascular evaluation, COPD,[5] pulmonary embolism[6]) to obtain quantitative data on bone quality without subjecting the patient to additional radiation exposure, cost, or time loss. Given the anatomical location of the L1 vertebra, which is included in the imaging field in the vast majority of thoracic and abdominal CT examinations, Hounsfield unit (HU)-based trabecular attenuation measurements derived from

this vertebral body have become an extremely ideal, practical, and reproducible biomarker for osteoporosis screening.[4,7] The literature emphasizes that low trabecular density of the L1 vertebra not only reflects current bone loss but also serves as an independent factor in predicting the risk of future osteoporotic fractures.[8,9]

The aim of this study is to investigate the effectiveness of opportunistic screening using measurements of trabecular density at the L1 vertebra in non-contrast chest CT scans routinely obtained for predicting the risk of osteoporosis and vertebral fractures, and to quantitatively assess the relationship between these measurements and clinical predictors such as age, gender, body-mass index (BMI), and chronic corticosteroid use.

METHODS

This study was conducted with the approval of the Necmettin Erbakan University Ethics Committee for Non-pharmaceutical and Non-medical Device Researches (Date: 27.02.2026, Decision No: 2026/6369). All procedures were carried out in accordance with the ethical rules and the principles of the Declaration of Helsinki. This study was designed as a retrospective, cross-sectional study to assess the risk of osteoporosis and vertebral fractures. Due to the retrospective nature of the study, the requirement for written informed consent was waived.

Adult patients (≥ 40 years of age) who underwent non-contrast chest CT scans for various clinical indications (predominantly suspected pulmonary infections, chronic obstructive pulmonary disease evaluation, and lung cancer screening) at the Radiology Clinic of Necmettin Erbakan University Hospital between January 1, 2024, and January 1, 2025, were retrospectively evaluated. During the initial radiological database screening, consecutive scans were reviewed, and patients were systematically excluded if they had severe vertebral deformity, metastatic lesions in the L1 vertebral body, hemangioma, a history of vertebroplasty, or severe metallic artifacts. Following this rigorous exclusion process, a final cohort of 385 eligible patients was established and included in the analysis. To ensure standardization and homogeneity in the imaging protocol, this study included non-contrast-enhanced chest CT scans acquired at a standard dose using a 256-slice dual-energy Siemens Somatom Drive CT scanner.

Measurements of trabecular density in the L1 vertebra were performed in accordance with the standard quantitative measurement methodology previously validated in the literature. The L1 vertebral body was clearly localized on reconstructed axial, coronal, and sagittal images of the patients. A standard elliptical region of interest (ROI) was placed at the mid-vertebral level within the anterior 1/3 trabecular area of the L1 vertebral body on axial images, carefully avoiding the cortical bone margins, the posterior venous plexus, and focal sclerotic bone islands (**Figure 1**). The mean attenuation values obtained from this region were recorded in HU.

To ensure measurement reliability, L1 trabecular attenuation values were measured independently by two radiologists.

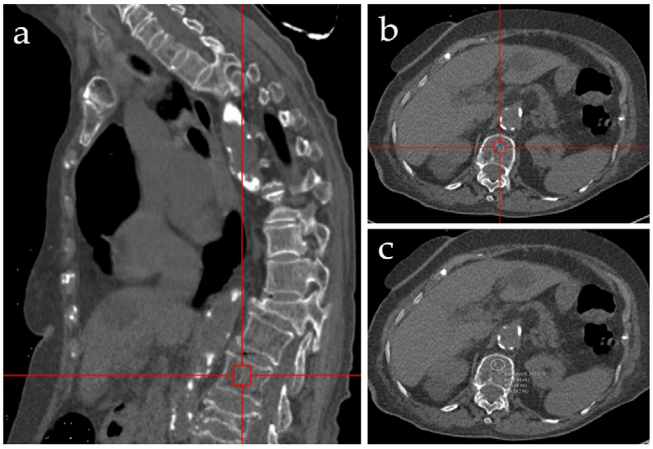

Figure 1. Measurement of L1 trabecular attenuation on non-contrast chest CT

The L1 vertebra is localized using sagittal (a) and axial (b) planes. An elliptical ROI is placed within the anterior trabecular bone (c) to obtain the mean HU value. CT: Computed tomography, ROI: Region of interest, HU: Hounsfield unit

The inter-observer agreement was excellent [intraclass correlation coefficient (ICC)=0.88]. The mean value of the two independent measurements was calculated and used for all subsequent statistical analyses.

The presence of VCF was assessed using sagittal CT reconstructions. In accordance with the Genant visual semi-quantitative (SQ) staging system, patients demonstrating a loss of at least 20% in normal vertebral height (Stage 1, mild fracture, or greater) were considered fracture-positive. Clinical data for the patients (age, gender, BMI, and history of systemic chronic corticosteroid use) were obtained from the hospital information management system.[10]

Statistical Analysis

The data were performed using SPSS v24.0 (IBM Corp., Armonk, NY, USA) and Jamovi v2.6 (Sydney, Australia). Statistical analyses were conducted by selecting tests appropriate for the distribution characteristics of the data. The normality of continuous variables was tested using the Shapiro-Wilk test. For variables showing a normal distribution, the independent samples t-test was applied; for those not showing a normal distribution, the Mann-Whitney U test was used. Categorical variables were expressed as frequencies and percentages and analyzed using the Chi-square test. Spearman's rank correlation analysis (rho) was used to determine the correlation between continuous variables. Univariate and multivariate logistic regression models were constructed to identify independent clinical factors predicting fracture risk. In the multivariate models, potential multicollinearity among variables was examined using the variance inflation factor (VIF) analysis. Receiver operating characteristic (ROC) analysis was performed to determine the diagnostic accuracy of the L1 HU measurement in distinguishing vertebral fractures and to identify the optimal cutoff value, and the Youden index was calculated. A p-value of <0.05 was considered statistically significant.

RESULTS

Study Population Characteristics

A total of 385 patients were included in the final analysis, comprising 231 female (60.0%) and 154 male (40.0%), with a mean age of 68.8±12.7 years (range: 44-90 years). The mean

BMI was 26.8±3.7 kg/m². Chronic corticosteroid use was documented in 36 patients (9.4%). The overall prevalence of vertebral fracture was 35.6% (n=137). The mean L1 vertebral trabecular attenuation measured on thoracic CT was 111.9±47.0 HU, with a median of 114 HU (interquartile range [IQR]: 70-154 HU). No missing data were present for any variable. A complete summary of baseline characteristics, stratified by fracture status, is presented in **Table 1**.

Table 1. Baseline demographic and clinical characteristics of the study population, stratified by vertebral fracture status

Variable	Overall (n=385)	VF-present (n=137)	VF-absent (n=248)	p-value
Age (years)	68.8±12.7	79.9±8.2	62.7±10.5	<0.001
Female gender, n (%)	231 (60.0)	130 (94.9)	101 (40.7)	<0.001
BMI (kg/m²)	26.8±3.7	26.1±3.6	27.2±3.6	0.006
Chronic steroid use, n (%)	36 (9.4)	28 (20.4)	8 (3.2)	<0.001
L1 vertebral density, H-mean±SD	111.9±47.0	71.2±35.1	134.4±36.6	<0.001
L1 vertebral density, HU-median (IQR)	114 (70-154)	62 (48-82)	138 (110-1629	<0.001

Continuous variables are expressed as mean±SD or median (IQR); categorical variables as n (%). Independent-samples t-test or Mann-Whitney U-test for continuous variables; Chi-square test for categorical variables. SD: Standard deviation, IQR: Interquartile range, VF: Vertebral fracture, BMI: Body-mass index, HU: Hounsfield units

Comparison of Clinical Variables Between Patients with and Without Vertebral Fracture

Patients who sustained a vertebral fracture were significantly older than those without fracture (79.9±8.2 vs. 62.7±10.5 years; t=16.640, p<0.001). BMI was modestly lower in the fracture group (26.1±3.6 vs. 27.2±3.6 kg/m²; p=0.006), although the magnitude of this difference was clinically limited.

A strikingly disproportionate gender distribution was observed across fracture groups. Vertebral fractures were present in 130 of 231 female (56.3%) but in only 7 of 154 male (4.5%), a difference that was highly statistically significant (χ^2=105.633, p<0.001). Chronic steroid use was more prevalent in fracture patients (20.4% vs. 3.2%; χ^2=28.847, p<0.001), conferring an unadjusted odds ratio (OR) of 7.71 (95% CI: 3.40-17.46).

L1 vertebral HU values were substantially lower in the fracture group [mean: 71.2±35.1 HU; median: 62 HU (IQR: 48-82)] than in the fracture-absent group [mean: 134.4±36.6 HU; median: 138 HU (IQR: 110-162)]. Given that Shapiro-Wilk testing confirmed non-normal distributions in both subgroups (p<0.001 for both), the Mann-Whitney U-test was applied and confirmed a highly significant difference (U=4013.5, p<0.001).

Association of L1 Vertebral HU with Clinical Variables

Spearman rank-order correlation revealed a strong inverse relationship between L1 vertebral HU and age (ρ=-0.952, p<0.001), indicating a progressive decline in trabecular bone density with advancing age in this cohort. A weak positive correlation was observed between L1 HU and BMI (r=0.164, p=0.001), while BMI itself did not emerge as a clinically dominant determinant of density in multivariable analyses.

Female patients exhibited significantly lower L1 HU values compared to males (94.5±48.9 HU vs. 138.0±28.5 HU; t=-9.949, p<0.001). Similarly, patients receiving chronic corticosteroid therapy had markedly lower trabecular attenuation than those without steroid exposure [median: 48 HU (IQR: 38-54) vs. 120 HU (IQR: 80-156); t=-9.008, p<0.001].

Vertebral Fracture Prevalence Across L1 HU-Based Density Categories

Patients were stratified into three clinically informative HU-based density categories. Among the 121 patients (31.4%) with severely reduced trabecular density (<80 HU), vertebral fractures were identified in 100 cases (82.6%). In the intermediate category (80-120 HU; n=90, 23.4%), fractures occurred in 24 patients (26.7%). In contrast, of the 174 patients (45.2%) with HU values exceeding 120, only 13 (7.5%) had sustained vertebral fractures. The gradient in fracture risk across these three strata was highly pronounced, underscoring the clinical utility of L1 HU as a categorical risk stratification tool. Fracture prevalence by HU category is detailed in **Table 2**.

Table 2. Vertebral fracture prevalence stratified by L1 trabecular density category

L1 HU category	n	VF-present, n (%)	VF-absent, n (%)
<80 HU (severely reduced)	121	100 (82.6)	21 (17.4)
80-120 HU (moderately reduced)	90	24 (26.7)	66 (73.3)
>120 HU (normal/mildly reduced)	174	13 (7.5)	161 (92.5)

HU: Hounsfield units, VF: Vertebral fracture

Logistic Regression Analyses for Vertebral Fracture Risk

In univariable logistic regression analyses, older age (OR=1.196; 95% CI: 1.154-1.239; p<0.001), female gender (OR=27.03; 95% CI: 12.13-60.25; p<0.001), chronic steroid use (OR=7.71; 95% CI: 3.40-17.46; p<0.001), and lower L1 HU (OR per HU=0.958; 95% CI: 0.951-0.966; p<0.001) were all significantly associated with vertebral fracture. Higher BMI was inversely associated with fracture risk in univariable analysis (OR=0.922; 95% CI: 0.869-0.977; p=0.006).

A multivariable logistic regression model incorporating all five predictors simultaneously yielded a Nagelkerke R^2 of 0.632 and an AUC of 0.911, indicating excellent overall discriminative capacity. However, VIF analysis revealed substantial multicollinearity between age and L1 vertebral HU (VIFage=29.3; VIFL1HU=11.2; VIFBMI=51.6), attributable to the near-perfect inverse correlation between these variables (Spearman ρ=-0.952). As a consequence, in the presence of age, the independent contributions of L1 HU (adjusted OR=0.994; 95% CI: 0.979-1.010; p=0.454), chronic steroid use (adjusted OR=0.865; 95% CI: 0.296-2.526; p=0.790), and BMI (adjusted OR=0.950; p=0.240) did not achieve statistical significance, while age (adjusted OR=1.119; 95% CI: 1.051-1.190; p<0.001) and female gender (adjusted OR=9.28; 95% CI: 3.87-22.25; p<0.001) remained independently significant. Full regression results are provided in **Table 3**.

Diagnostic Performance of L1 Vertebral HU for Vertebral Fracture Prediction

ROC analysis demonstrated that L1 vertebral HU measurement alone provided strong discriminative

Table 3. Univariable and multivariable logistic regression analysis of factors associated with vertebral fracture

Variable	Univariable OR (95% CI)		Adjusted OR (95% CI)*	p-value (adj.)
	OR (95% CI)	p-value		
Age (per year)	1.196 (1.154-1.239)	<0.001	1.119 (1.051-1.190)	<0.001
Female gender	27.03 (12.13-60.25)	<0.001	9.28 (3.87-22.25)	<0.001
BMI (per kg/m²)	0.922 (0.869-0.977)	0.006	0.950 (0.873-1.035)	0.240
Chronic steroid use	7.706 (3.402-17.46)	<0.001	0.865 (0.296-2.526)†	0.790
L1 vertebral density (per HU)	0.958 (0.951-0.966)	<0.001	0.994 (0.979-1.010)†	0.454

Reference categories: male gender; no steroid use. *Adjusted for all listed covariates simultaneously. †Significance attenuated by high multicollinearity with age (VIF>10). OR: Odds ratio, CI: Confidence interval, BMI: Body-mass index, HU: Hounsfield units, VIF: Variance inflation factor, NS: Not significant

performance for vertebral fracture prediction, with an area under the curve (AUC) of 0.882 (95% CI: 0.843-0.921) (**Figure 2**). The Youden index identified an optimal HU threshold of 94 HU, at which the sensitivity was 86.9%, specificity was 89.1%, positive predictive value (PPV) was 81.5%, negative predictive value (NPV) was 92.5%, and overall diagnostic accuracy was 88.3%. The full multivariable model achieved an AUC of 0.911, representing a modest absolute increment over the single-parameter L1 HU measure. Diagnostic performance metrics at the optimal threshold are summarized in **Table 4**.

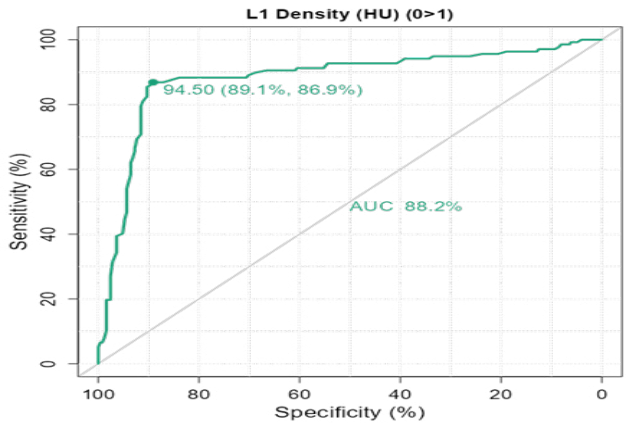

Figure 2. ROC curve evaluating the performance of L1 trabecular density in predicting vertebral fracture

The optimal threshold of 94 HU demonstrates a sensitivity of 86.9% and a specificity of 89.1% (AUC=0.882). HU: Hounsfield unit, AUC: Area under the receiver operating characteristic curve, ROC: Receiver operating characteristic

Table 4. Diagnostic performance characteristics of L1 vertebral HU measurement for the prediction of vertebral fracture at the Youden-optimal threshold of 94 HU

Parameter	Value	95% CI
AUC (L1 HU alone)	0.882	0.843-0.921
AUC (full multivariable model)	0.911	—
Optimal cut-off (Youden index)	94 HU	—
Sensitivity	86.9%	—
Specificity	89.1%	—
Positive predictive value (PPV)	81.5%	—
Negative predictive value (NPV)	92.5%	—
Overall accuracy	88.3%	—

The full multivariable model AUC (0.911) is provided for comparison. HU: Hounsfield unit, CI: Confidence interval, AUC: Area under the receiver operating characteristic curve, PPV: Positive predictive value, NPV: Negative predictive value

DISCUSSION

Our study suggests that the HU density of the L1 vertebra is a reliable and useful biomarker for predicting the presence of fractures in an aging population among individuals who have undergone non-contrast chest CT scans for various indications.

Although the HU thresholds defined in the literatüre for opportunistic CT scans vary, our findings are largely consistent with leading reference studies. In a large-scale cohort study, Pickhardt and colleagues[7] determined that the optimal L1 attenuation value for detecting osteoporosis is 100 HU; sensitivity and specificity were found to be high at this threshold. Additionally, in another study investigating vertebral fractures,[11] the threshold value was determined to be 95 HU. The 94 HU value identified in our cohort nearly matches literature, suggesting the potential consistency of this metric, although prospective external validation is necessary to truly confirm its reproducibility across different populations.

In a normative data study by Jang et al.[12] involving more than 20.000 adults, it was found that L1 trabecular attenuation exhibited a linear decrease of 2.5 HU per year of age. In our cohort as well, age stratification analysis showed that the mean, which was 165 HU in patients under 60 years of age, dropped sharply to 50 HU in those over 80 years of age. A critical statistical finding in our study was the substantial multicollinearity observed between age and L1 attenuation (r=-0.952, VIF>10). Because trabecular bone density physiologically declines with advancing age, these two variables share highly overlapping variance in predicting fracture risk. Consequently, when both were included in the multivariable regression model, L1 HU lost its independent statistical significance. However, from a clinical perspective, this does not diminish the value of L1 HU. Rather than viewing L1 HU as a strictly independent risk factor, it should be interpreted as a quantifiable imaging biomarker that physically manifests and measures the extent of age-related bone deterioration. In opportunistic screening, L1 HU provides an objective, patient-specific metric of bone quality that chronological age alone cannot visually demonstrate.

The fact that female patients have a dramatically higher fracture rate compared to male and that their average HU values are significantly lower reflects the accelerated destructive effects of postmenopausal estrogen deficiency on bone microarchitecture.[13] The identification of female gender as an independent factor increasing fracture risk in our study further supports the necessity of prioritizing postmenopausal women as the primary target population in osteoporosis screening.

In our study, the decline in L1 trabecular density to low levels and the associated increased risk of fracture in patients receiving chronic steroid therapy may serve as a critical strategy for this patient group to incorporate opportunistic chest CT scans into routine follow-up, enabling the early detection of subclinical fractures and prompting further formal clinical evaluation (e.g., DXA referral) for the consideration of prophylactic anti-osteoporotic treatments.

Limitations

This study has several limitations that should be taken into account. First, since the study has a retrospective, cross-sectional, and single-center design, it is not possible to definitively establish a temporal causal relationship between decreasing HU values and the development of fractures. Additionally, the retrospective recruitment based on specific clinical indications introduces potential selection bias. Furthermore, the profound multicollinearity between age and L1 attenuation limits our ability to evaluate the truly independent contribution of trabecular density in multivariable prediction models. Second, the lack of concurrent DXA (T-score) data for the patients prevented a direct correlation between HU values and standard BMD scores. Third, a marked gender imbalance was present in our cohort, with a disproportionately high number of female in the fracture group; thus, the findings should be interpreted with caution when applied to male populations. Fourth, all scans included in the study were performed using the same specific CT scanner. The literature indicates that HU values detected in opportunistic scans may exhibit certain degrees of variation depending on the manufacturer, device generation, and scanning protocols. Finally, the optimal ROC cutoff value of 94 HU was derived and evaluated within the same cohort. This approach can lead to optimistic diagnostic performance estimates, underscoring the critical need for external validation. Therefore, caution is warranted when directly generalizing the findings of our study to other device ecosystems or unvalidated populations.

Our recommendations for future studies are to calibrate and validate the identified diagnostic thresholds using large-scale, prospective cohorts that include multiple institutions and different brands/models of CT systems. Additionally, performing L1 vertebral ROI delineation using AI-based automatic segmentation and deep learning algorithms without the need for human intervention will be an essential step toward seamlessly integrating opportunistic screening into the clinical workflow without increasing the workload of radiologists.

CONCLUSION

As a result, the measurement of trabecular density at the L1 vertebra derived from non-contrast chest CT scans is a useful, time-efficient, and non-invasive opportunistic screening tool for predicting the presence of osteoporosis and the risk of vertebral compression fractures.

ETHICAL DECLARATIONS

Ethics Committee Approval

This study was conducted with the approval of the Necmettin Erbakan University Ethics Committee for Non-Pharmaceutical and Non-medical Device Researches (Date: 27.02.2026, Decision No: 2026/6369).

Informed Consent

As this was a retrospective study, formal written informed consent was not required and was therefore not obtained. This retrospective study used pre-existing anonymized patient data. No additional intervention was performed, and there was no direct patient contact. The study was approved by the Ethics Committee, and the requirement for written informed consent was waived by the ethics committee.

Peer Review Process

This manuscript was subject to external peer review.

Conflict of Interest

The authors declare no conflicts of interest related to this study.

Financial Disclosure

The authors received no financial support for the conduct or publication of this research.

Author Contributions

Conceptualization: HE; Methodology: HE, HEK; Data Collection: HE, HEK; Formal Analysis: HE, AEA; Writing the Manuscript: HE; Writing-Review and Editing: AEA; Supervision: AEA, HEK.

REFERENCES

1. Vadera S, Osborne T, Shah V, Stephenson JA. Opportunistic screening for osteoporosis by abdominal CT in a British population. *Insights Imaging*. 2023;14(1):57. doi:10.1186/s13244-023-01400-1
2. Angeli A, Guglielmi G, Dovio A, et al. High prevalence of asymptomatic vertebral fractures in post-menopausal women receiving chronic glucocorticoid therapy: a cross-sectional outpatient study. *Bone*. 2006; 39(2):253-259. doi:10.1016/j.bone.2006.02.005
3. Zou D, Li W, Deng C, Du G, Xu N. The use of CT Hounsfield unit values to identify the undiagnosed spinal osteoporosis in patients with lumbar degenerative diseases. *Eur Spine J*. 2019;28(8):1758-1766. doi:10.1007/s00586-018-5776-9
4. Patel N, Dahl K, O'Rourke R, et al. Vertebral CT attenuation outperforms standard clinical fracture risk prediction tools in detecting osteoporotic disease in lung cancer screening participants. *Br J Radiol*. 2023;96(1151):20220992. doi:10.1259/bjr.20220992
5. Koç A, Ataş AE. Relationship between pulmonary artery-to-aorta ratio and hospital length of stay in chronic obstructive pulmonary disease exacerbations: a retrospective cohort analysis and clinical implications. *J Health Sci Med*. 2026;9(1):45-51. doi:10.32322/jhsm.1794663
6. Koc A, Vatansev H. Prognostic relevance of biochemical markers integrated with simplified pulmonary embolism severity index in acute pulmonary embolism. *Ann Clin Anal Med*. 2025;16(12):893-898. doi:10.4328/acam.22700
7. Pickhardt PJ, Pooler BD, Lauder T, del Rio AM, Bruce RJ, Binkley N. Opportunistic screening for osteoporosis using abdominal computed tomography scans obtained for other indications. *Ann Intern Med*. 2013;158(8):588-595. doi:10.7326/0003-4819-158-8-201304160-00003
8. Guenoun D, Champsaur P. Opportunistic computed tomography screening for osteoporosis and fracture. *Semin Musculoskelet Radiol*. 2023;27(4):451-456. doi:10.1055/s-0043-1771037
9. Lee SJ, Graffy PM, Zea RD, Ziemlewicz TJ, Pickhardt PJ. Future osteoporotic fracture risk related to lumbar vertebral trabecular attenuation measured at routine body CT. *J Bone Miner Res*. 2018;33(5): 860-867. doi:10.1002/jbmr.3383
10. Genant HK, Wu CY, van Kuijk C, Nevitt MC. Vertebral fracture assessment using a semiquantitative technique. *J Bone Miner Res*. 1993; 8(9):1137-1148. doi:10.1002/jbmr.5650080915
11. Zhang SB, Xu HW, Yi YY, Hu T, Wang SJ, Wu DS. Evaluation of the use of CT attenuation for the prediction of subsequent vertebral fracture in patients with osteoporosis. *Pain Physician*. 2021;24(4):E493-E500.
12. Jang S, Graffy PM, Ziemlewicz TJ, Lee SJ, Summers RM, Pickhardt PJ. Opportunistic osteoporosis screening at routine abdominal and thoracic CT: normative L1 trabecular attenuation values in more than 20 000 adults. *Radiology*. 2019;291(2):360-367. doi:10.1148/radiol.2019181648
13. Khosla S, Monroe DG. Regulation of bone metabolism by sex steroids. *Cold Spring Harb Perspect Med*. 2018;8(1):a031211. doi:10.1101/cshperspect.a031211

Journal of Radiology Medicine in

Case Report

Doi: 10.51271/JRM-0054

Type 2B torcular Herophili variant in a two-week-old neonate: MR venography findings

Mehmet Haydar Atalar*, Serdar Aktı, Nisa Başpınar

Division of Neuroradiology, Department of Radiology, Faculty of Medicine, Sivas Cumhuriyet University, Sivas, Turkiye

Received: 06.06.2026 ◆ **Accepted**: 27.07.2026 ◆ **Published**: 19.09.2026

Cite this article: Atalar MH, Aktı S, Başpınar N. Type 2B torcular Herophili variant in a two-week-old neonate: MR venography findings. *J Radiol Med.* 2026;3(3):71-73. doi:10.51271/JRM-0054

***Corresponding Author:** Mehmet H. Atalar, mhatalar@gmail.com

ABSTRACT

The torcular Herophili (confluence of sinuses) shows considerable anatomical variation. Type 2B torcular Herophili is an uncommon configuration characterized by preferential drainage of the straight sinus into the right transverse sinus. Recognizing this variant is important to avoid misinterpretation on magnetic resonance venography (MRV). We report a two-week-old male neonate in whom an incidental torcular Herophili variant was identified on brain MRI and MRV. MRV demonstrated preferential drainage of the straight sinus into a dominant right transverse sinus, while the left transverse sinus was smaller but patent. According to the Kobayashi classification, this finding corresponded to a type 2B torcular Herophili variant. Based on the Gökçe classification, the same configuration was consistent with a type IIA2 partial confluence pattern. This case highlights the importance of recognizing normal torcular Herophili variants in neonatal MRV and differentiating them from pathological conditions such as transverse sinus hypoplasia or cerebral venous sinus thrombosis.

Keywords: Torcular Herophili, confluence of sinuses, MR venography, neonate, dural venous sinus variant, anatomical variation

INTRODUCTION

The torcular Herophili, or confluence of sinuses, is a key anatomical region of the intracranial venous system located near the internal occipital protuberance. It is the junction of the superior sagittal sinus, straight sinus, transverse sinuses, and, variably, the occipital sinus. Although often depicted as a symmetric venous confluence, considerable anatomical variability has been documented in both anatomical and radiological studies.[1-3]

Variations of the torcular Herophili may involve differences in venous drainage patterns, transverse sinus dominance, and the degree of confluence between major dural venous sinuses. These configurations usually represent normal anatomical variants but may occasionally mimic pathological conditions on magnetic resonance venography (MRV), particularly when asymmetrical venous drainage is present.[1,3,4]

Type 2B torcular Herophili is an uncommon configuration characterized by preferential drainage of the straight sinus into the right transverse sinus.[1] Recognition of such variants is important for accurate interpretation of MRV and to avoid diagnostic confusion with venous sinus abnormalities.

We describe the MR venographic findings of a rare torcular Herophili variant in a two-week-old male neonate, detected incidentally on MR venography, and discuss its classification according to the Kobayashi and Gökçe systems. The purpose of this report is to describe the imaging appearance of this venous confluence configuration, clarify its classification according to both the Kobayashi and Gökçe systems, and emphasize the importance of neutral anatomical interpretation in neonatal MR venography.

CASE

A two-week-old male neonate was referred for brain MRI and MRV because of intermittent irritability and concern for possible intracranial pathology. Physical examination was unremarkable, and no focal neurological deficit was identified. Routine laboratory investigations, including coagulation parameters, were within normal limits. MRI and MRV were requested primarily to exclude cerebral venous sinus thrombosis or other intracranial abnormalities. No previously known intracranial vascular malformation was reported. Brain MRI and MRV were performed on a 1.5-T scanner using a standard neonatal imaging protocol. The examination included axial and sagittal T1-weighted imaging,

axial T2-weighted imaging, diffusion-weighted imaging, susceptibility-weighted imaging, and three-dimensional time-of-flight (3D TOF) MR venography. Maximum intensity projection (MIP) and three-dimensional volume-rendered reconstructions were generated for evaluation of the dural venous sinuses. Conventional MRI showed no acute parenchymal abnormality, restricted diffusion, intracranial hemorrhage, hydrocephalus, or mass effect. A rare torcular Herophili configuration was identified. The straight sinus drained preferentially into the right transverse sinus rather than forming a symmetric central venous confluence. The right transverse sinus was dominant, while the left transverse sinus was relatively smaller in caliber but remained patent (**Figure**).

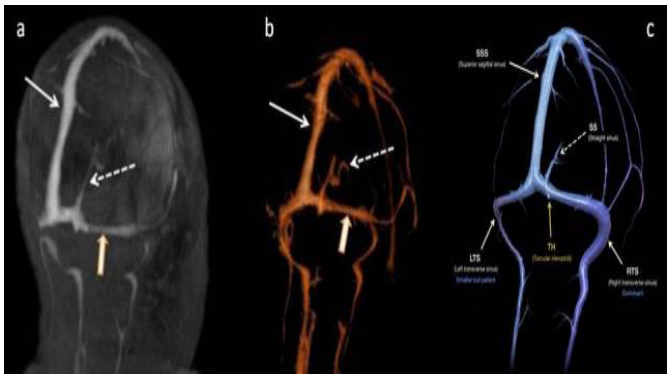

Figure. MRV demonstrating the torcular Herophili configuration

(A) Maximum intensity projection and (B) three-dimensional volume-rendered MRV images show preferential drainage of the straight sinus (dashed white arrows) into the right transverse sinus (solid arrow). The right transverse sinus is dominant, and the torcular confluence is indicated by white arrows. The left transverse sinus is relatively smaller but patent. This pattern corresponds to type 2B in the Kobayashi classification and type IIA2 partial confluence in the Gökçe classification. (C) Three-dimensional schematic illustration of the venous anatomy in the present neonate, showing preferential drainage of the SS into the dominant RTS, with a smaller but patent LTS. The SSS joins the torcular TH, and venous continuity is preserved. SSS: Superior sagittal sinus, SS: Straight sinus, LTS: left transverse sinus, RTS: Right transverse sinus, MRV: Magnetic resonance venography, Th: Herophili

According to the classification proposed by Kobayashi et al.,[1] this configuration corresponded to a type 2B torcular Herophili variant. According to the classification of Gökçe et al.,[4] the same venous anatomy was most consistent with a type IIA2 partial confluence pattern, as the superior sagittal sinus and straight sinus drained separately into the transverse sinus system while maintaining normal venous continuity. The imaging findings were interpreted as an incidental anatomical variant without evidence of venous sinus thrombosis or other intracranial abnormality. The finding was documented in the radiology report as a normal variation of dural venous sinus anatomy for future reference. Ethical approval was waived by the institutional review board because this study represents a single anonymized case report. Written informed consent for publication of clinical and imaging data was obtained from the patient's parents.

DISCUSSION

The torcular Herophili is one of the most anatomically variable regions of the intracranial venous system. Although classical anatomical descriptions depict a symmetric confluence of the superior sagittal sinus, straight sinus, and bilateral transverse sinuses, numerous anatomical and radiological studies have demonstrated considerable variability in venous drainage patterns, transverse sinus dominance, and the degree of confluence between the major dural venous sinuses. These configurations usually represent normal developmental variants rather than pathological abnormalities and should be recognized during routine MR venography.[1-4]

Kobayashi et al.[1] systematically evaluated the confluence of sinuses using contrast-enhanced MR venography and demonstrated several reproducible drainage patterns, including preferential drainage of the straight sinus into one transverse sinus. Gökçe et al.[4] further expanded this concept by proposing a practical classification system based on MR venography and digital subtraction angiography, emphasizing that preservation of venous continuity is the key feature distinguishing anatomical variants from pathological conditions. Bayaroğulları et al.[3] similarly showed that asymmetric transverse sinus drainage is common in pediatric MR venography and generally reflects normal developmental anatomy rather than disease.

The venous anatomy observed in the present neonate corresponds to a Kobayashi[1] type 2B torcular Herophili configuration and a Gökçe[4] type IIA2 partial confluence pattern. Bayaroğulları et al.[3] evaluated pediatric MR venography and demonstrated that asymmetric transverse sinus drainage commonly represents a normal developmental variant; however, they did not specifically illustrate a neonatal Kobayashi type 2B configuration. Similarly, the studies by Kobayashi et al.[1] and Gökçe et al.[4] primarily evaluated adult populations or mixed-age cohorts rather than neonates. Although this anatomical configuration has been incorporated into established classification systems, reports specifically illustrating this variant during the neonatal period remain exceptionally limited. To our knowledge, no previous publication has provided a dedicated MR venographic illustration of a Kobayashi type 2B torcular Herophili configuration in a neonate. Although similar anatomical variants have been included within broader pediatric series, the principal contribution of the present report is not the identification of a new anatomical variant but the demonstration that this configuration can already be recognized during the neonatal period using routine MR venography, thereby extending the documented age spectrum of this recognized venous anatomy.

Recognition of this venous anatomy has important practical implications. Neonatal MR venography is frequently performed to exclude cerebral venous sinus thrombosis in infants presenting with nonspecific neurological symptoms. In this setting, asymmetric venous drainage or transverse sinus dominance may be incorrectly interpreted as transverse sinus hypoplasia or venous thrombosis if normal anatomical variants are not considered.[1,3-5] In the present case, the straight sinus drained preferentially into the dominant right transverse sinus, whereas the left transverse sinus was smaller but remained patent, without associated parenchymal abnormalities or imaging findings suggestive of thrombosis. Preservation of venous continuity and the absence of secondary MRI abnormalities supported the diagnosis of a normal developmental variant rather than pathology.

Beyond diagnostic interpretation, accurate recognition of torcular Herophili variants is relevant for neurosurgical planning, posterior fossa interventions, endovascular procedures, and longitudinal radiological follow-up. Recent

cadaveric investigations have also demonstrated substantial morphological diversity of the dural venous sinuses, reinforcing that considerable variability represents normal anatomy rather than pathological alteration. Knowledge of individual venous drainage patterns facilitates appropriate interpretation of future neurovascular imaging studies and reduces the likelihood of unnecessary investigations or inappropriate treatment. Anatomical case reports describing uncommon torcular configurations, including circular torcular Herophili and other rare drainage patterns, further illustrate the wide spectrum of normal venous anatomy.[2,6,7]

A systematic assessment of the torcular region may improve diagnostic confidence on MR venography. Important imaging features include the drainage pattern of the straight sinus, drainage of the superior sagittal sinus, transverse sinus dominance, preservation of venous continuity, the presence of an occipital sinus or accessory venous channels, and the absence of secondary imaging findings suggesting venous obstruction.[1,3,4] Such a structured approach is particularly valuable in neonatal and pediatric imaging, where developmental asymmetry and relatively small venous caliber may complicate interpretation.

The present report has several limitations. It describes a single incidental anatomical observation without long-term imaging follow-up, and no additional vascular imaging such as contrast-enhanced MR venography, CT venography, or digital subtraction angiography was performed because these investigations were not clinically indicated. Nevertheless, routine brain MRI combined with three-dimensional time-of-flight MR venography adequately demonstrated the characteristic venous drainage pattern and allowed confident classification according to both the Kobayashi and Gökçe systems.

CONCLUSION

The present case demonstrates that a Kobayashi type 2B/Gökçe type IIA2 torcular Herophili configuration can be readily identified on routine MR venography during the neonatal period. Although this represents a recognized anatomical variant rather than a new entity, its dedicated MR venographic documentation expands the documented age spectrum of this normal venous configuration and reinforces its relevance in neonatal neuroimaging. Awareness of this anatomical variant, together with systematic evaluation of venous continuity and drainage patterns, may help avoid misdiagnosis of cerebral venous sinus thrombosis or transverse sinus hypoplasia, improve diagnostic confidence, and support appropriate clinical management.

ETHICAL DECLARATIONS

Informed Consent

Informed consent was obtained from the legal guardians of the pediatric patient described in this report. Where developmentally appropriate, assent was also sought from the child.

Peer Review Process

This report underwent external peer review.

Conflict of Interest

The authors declare no conflicts of interest.

Financial Disclosure

This case report did not receive any financial support.

Author Contributions

Concept: MHA, SA, NB; Design: MHA, SA, NB; Control: MHA, SA, NB; Data Collection and/or Processing: MHA, SA, NB; Analysis and/or Interpretation: MHA, SA, NB; Literature Review: MHA, SA, NB; Article Writing: MHA, SA, NB; Critical Review: MHA, SA, NB.

REFERENCES

1. Kobayashi K, Matsui O, Suzuki M, Ueda F. Anatomical study of the confluence of the sinuses with contrast-enhanced magnetic resonance venography. *Neuroradiology*. 2006;48(5):307-311. doi:10.1007/s00234-006-0065-4
2. Lake S, Altafulla JJ, Iwanaga J, Oskouian RJ, Loukas M, Tubbs RS. A cadaveric case of a circular torcular Herophili. *Cureus*. 2018;10(8):e3099. doi:10.7759/cureus.3099
3. Bayaroğulları H, Burakgazi G, Duman T. Evaluation of dural venous sinuses and confluence of sinuses via MRI venography: anatomy, anatomic variations, and the classification of variations. *Childs Nerv Syst*. 2018;34(6):1183-1188. doi:10.1007/s00381-018-3763-4
4. Gökçe E, Pınarbaşılı T, Acu B, Fırat MM, Erkorkmaz Ü. Torcular Herophili classification and evaluation of dural venous sinus variations using digital subtraction angiography and magnetic resonance venographies. *Surg Radiol Anat*. 2014;36(6):527-536. doi:10.1007/s00276-013-1223-0
5. Paudel S, Sah R, Singh RK, Kayastha P, Katwal S. Dural venous sinus variations observed in magnetic resonance venography at a tertiary care hospital: an observational study. *JNMA J Nepal Med Assoc*. 2024; 62(279):720-724. doi:10.31729/jnma.8795
6. Casaperalta GL, Medina CAL. Type 4A torcular Herophili anatomic variant detected by cerebral digital subtraction angiography: case report. *Surg Radiol Anat*. 2026;48(1):106. doi:10.1007/s00276-026-03877-z
7. Kamaşak Arpaçay B, Aycan K. Morphological variations of the dural venous sinuses: a cadaveric study. *Front Surg*. 2026;13:1800026. doi:10.3389/fsurg.2026.1800026

Journal of Radiology Medicine in

Case Report

Doi: 10.51271/JRM-0055

Anomalous drainage of the great cardiac vein into the left atrial appendage: a two-case report

Mehmet Ali Kaptan*, Alptuğ Özen

Department of Radiology, Mersin City Training and Research Hospital, Mersin Turkiye

Received: 16.06.2026 ◆ **Accepted**: 01.09.2026 ◆ **Published**: 19.09.2026

Cite this article: Kaptan MA, Özen A. Anomalous drainage of the great cardiac vein into the left atrial appendage: a two-case report. *J Radiol Med.* 2026;3(3):74-79. doi:10.51271/JRM-0055

***Corresponding Author:** Mehmet Ali Kaptan, mealikaptan@gmail.com

ABSTRACT

Coronary venous system anomalies are rare structural variants that are usually detected incidentally. The great cardiac vein (GCV) normally drains into the coronary sinus (CS) through the valve of Vieussens, returning venous blood to the right atrium. Direct drainage of the GCV into the left atrial appendage (LAA) is an extremely rare anomaly, described in only a few reports. We present two female patients, aged 50 and 53 years, who underwent coronary computed tomography angiography (CCTA) for chest pain and in whom anomalous drainage of the GCV into the LAA was detected incidentally; in neither patient could a connection with the CS be demonstrated. Both patients were referred to cardiology; no intervention was indicated and clinical surveillance was recommended. At one year of follow-up neither had developed further cardiac symptoms, documented atrial arrhythmia or thromboembolic complications, and longer-term follow-up was not available. CCTA allowed the anomaly to be recognised and mapped three-dimensionally in both patients. Recognition of the anomaly is relevant to the planning of LAA-targeted interventions, transseptal approaches and coronary sinus-related procedures.

Keywords: Great cardiac vein, left atrial appendage, coronary venous anomaly, coronary computed tomography angiography, coronary sinus

INTRODUCTION

Anomalies of the cardiac venous system are rare congenital variations that usually follow an asymptomatic course and are detected incidentally during the investigation of other cardiac conditions.[1-3] Most of the coronary venous system drains into the right atrium through the coronary sinus (CS), which lies in the posterior left atrioventricular groove and opens into the right atrium adjacent to the orifice of the inferior vena cava.[1,4] The great cardiac vein (GCV) is the principal pathway of this drainage: it arises at the cardiac apex in the anterior interventricular sulcus, ascends parallel to the left anterior descending (LAD) artery, turns into the left atrioventricular groove alongside the left circumflex (LCx) artery, and continues as the CS at the level of the valve of Vieussens.[4,5]

The coronary venous system develops from the sinus venosus between the fifth and eighth weeks of gestation. As systemic venous return shifts progressively to the right, the left horn of the sinus venosus and the left common cardinal vein regress: the persisting proximal portion of the left sinus horn becomes the CS, whereas the obliterated left common cardinal vein persists as the oblique vein of the left atrium (vein of Marshall) and its fibrous remnant, the ligament of Marshall.[1,6,7] In parallel, the subepicardial venous plexus draining the developing myocardium establishes continuity with the CS. Failure of regression of the left cardinal system produces a persistent left superior vena cava (PLSVC); failure of separation between the CS and the left atrium produces an unroofed CS; and persistence of primitive connections between the subepicardial plexus and the left atrium-or failure of the GCV to establish continuity with the CS-may lead to coronary venous blood draining directly into the left atrium or the left atrial appendage (LAA).[1,2,8,9]

The spectrum of coronary venous anomalies also includes CS ostial atresia or stenosis, an absent or hypoplastic CS, and anomalous communications with the left-sided chambers.[1-3,5] Direct drainage of the GCV into the LAA is among the rarest of these variants and has, to our knowledge, been documented only in isolated case reports.[10-12]

We describe two patients in whom the GCV drained directly into the LAA with no demonstrable connection to the CS. We report the CCTA acquisition protocol and quantitative anatomical data, define the features that distinguish this anomaly from other vascular structures related to the LAA, and compare the two cases in order to illustrate the morphological variability of the entity.

CASE

Imaging Technique

All examinations were performed on a 64-detector-row CT scanner (Optima CT660, GE Healthcare, Milwaukee, WI, USA). Heart rate was controlled with oral metoprolol 50 mg once daily for five days before the examination and a further 50 mg 1-2 hours before scanning. Contrast-enhanced images were acquired with retrospective ECG gating after intravenous administration of 100 ml of iodinated contrast medium (Kopaq, 350 mg I/ml) through a right antecubital vein at a flow rate of 5 ml/s, followed by a saline chaser. Images were reconstructed at a section thickness of 0.625 mm over the 40-75% R-R interval. Post-processing included multiplanar and curved multiplanar reformation (cMPR), maximum intensity projection (MIP) and volume rendering (VR) on a dedicated GE AW workstation. Both examinations were reviewed in consensus by two radiologists with ten years' experience in cardiac imaging. Acquisition and reporting followed the recommendations of the Society of Cardiovascular Computed Tomography.[13,14]

Case 1

A 50-year-old female was referred for CCTA after cardiology assessment for atypical chest pain occurring both on exertion and at rest. She had no known coronary artery disease, hypertension or diabetes mellitus, and physical examination showed no cardiovascular abnormality.

Transthoracic echocardiography (TTE) showed a left ventricular ejection fraction (EF) of 60%, with no regional wall motion abnormality, valvular pathology or pericardial effusion. Cardiac biomarkers (high-sensitivity troponin I, CK-MB) and all other laboratory parameters were normal.

CCTA showed no obstructive coronary artery stenosis and was reported as CAD-RADS 1/E.[14] The LAD showed myocardial bridging in the anterior interventricular sulcus over a length of approximately 28 mm, with a superficial intramyocardial depth of 1-2 mm (**Figure 1**).

Evaluation of the venous system revealed a coronary venous drainage anomaly: the GCV ascended in the anterior interventricular sulcus alongside the LAD, continued into the left atrioventricular groove and terminated in the LAA instead of continuing as the CS (**Figure 2-4**). A thin-walled CS, approximately 2 mm in diameter, lay in the posterior atrioventricular groove and drained the mid- to distal-segment coronary veins (such as the middle cardiac vein and the posterior vein of the left ventricle) into the right atrium. No connection between the CS and the GCV was seen (**Figures 5** and **6**).

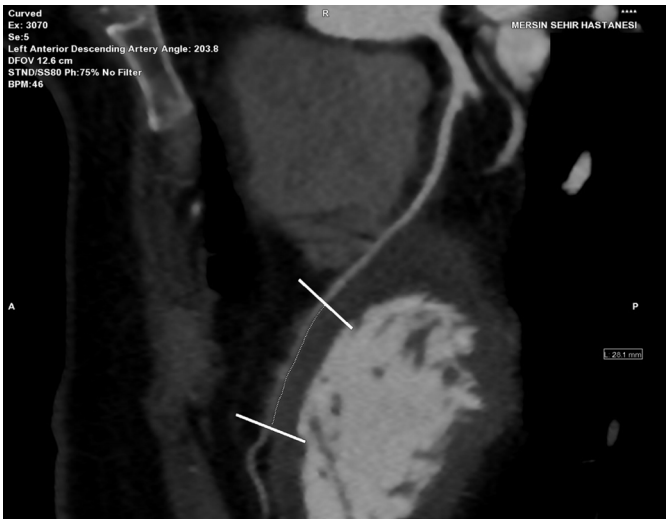

Figure 1. Case 1. cMPR CT image showing superficial myocardial bridging of the LAD coronary artery (28 mm in length, 1-2 mm intramyocardial depth)

DFOV: Display field of view, BPM: Beats per minute, cMPR: Curved multiplanar reformation, CT: Computed tomography, LAD: Left anterior descending

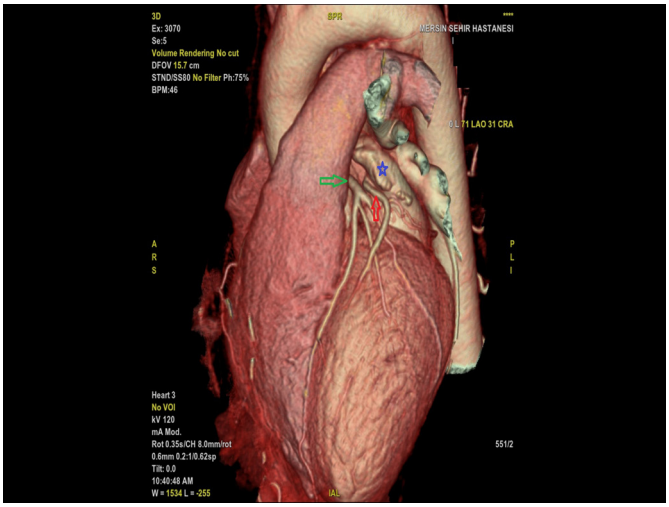

Figure 2. Case 1. Three-dimensional volume-rendered CT image. Blue star: LAA; red arrow: GCV; green arrow: left main coronary artery. The GCV terminates directly in the LAA

DFOV: Display field of view, BPM: Beats per minute, kV: Kilovolt, mA: Milliampere, Mod.: Modulation, Rot: Rotation, s: Second, mm: Millimeter, CH: Channel, sp: Spacing, AM: Ante meridiem, W: Window width, L: Window level, Vol: Volume, VOI: Volume of interest, LAO: Left anterior oblique, CRA: Cranial, LAA: left atrial appendage, GCV: Great cardiac vein

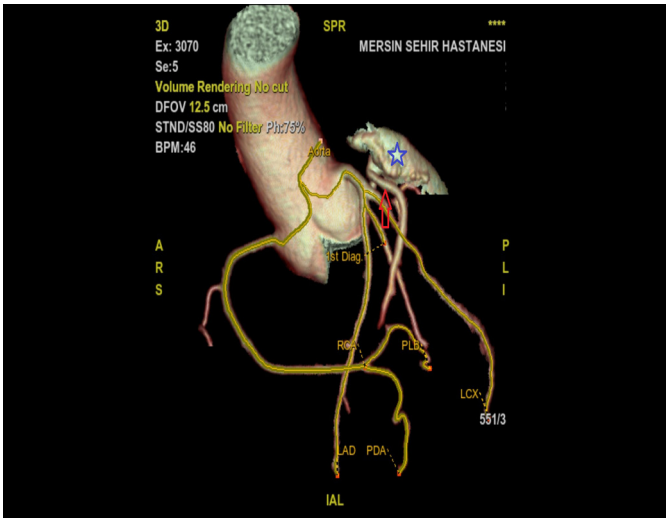

Figure 3. Case 1. Three-dimensional volume-rendered CT image in a complementary projection. Blue star: LAA; red arrow: GCV; green arrow: left main coronary artery

3D: Three-dimensional, Ex: Examination, Se: Series, SPR: Superior-posterior-right, DFOV: Display field of view, STND: Standard, Ph: Phase, BPM: Beats per minute, RCA: Right coronary artery, PLB: Posterolateral branch, LCX: Left circumflex artery, LAD: Left anterior descending artery, PDA: Posterior descending artery, CT: Computed tomography, LAA: left atrial appendage, GCV: Great cardiac vein

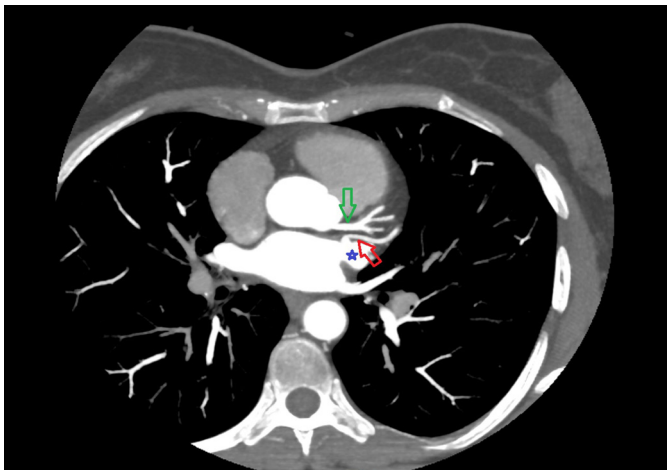

Figure 4. Case 1. Axial CT image. Blue star: LAA; red arrow: GCV; green arrow: left main coronary artery
CT: Computed tomography, LAA: left atrial appendage, GCV: Great cardiac vein

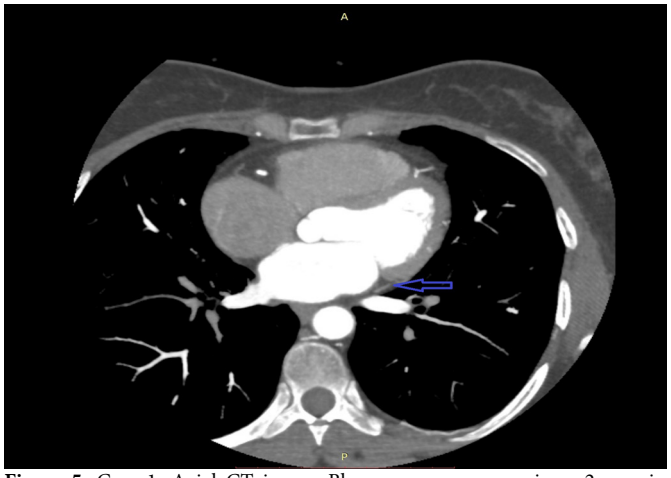

Figure 5. Case 1. Axial CT image. Blue arrow: coronary sinus, 2 mm in diameter, in the posterior atrioventricular groove
CT: Computed tomography

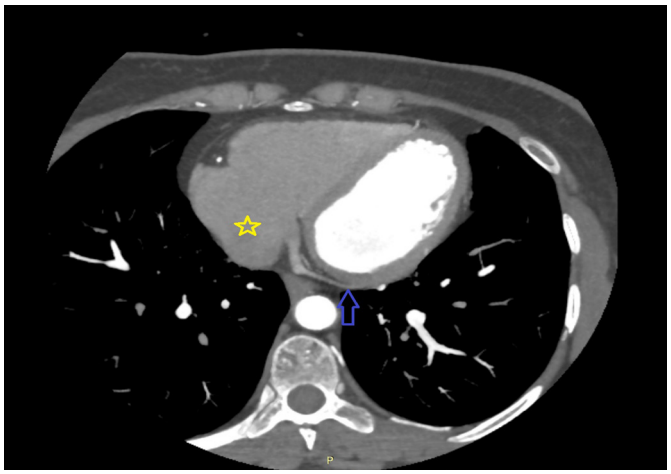

Figure 6. Case 1. Axial CT image, consecutive section following Figure 5. Blue arrow: coronary sinus; yellow star: right atrium
CT: Computed tomography

Quantitative measurements: the GCV measured 2.2 mm in the anterior interventricular sulcus and 2.3 mm immediately proximal to its termination in the LAA. The anomalous segment, measured from the point at which the vessel left the expected course of the CS to its termination, was 60 mm long. Because the study was acquired in the arterial phase, all venous measurements were taken along the segment in which luminal contrast filling of the vein could be followed, and the reported length corresponds to this opacified segment. The LAA was of chicken-wing morphology, with maximum dimensions (AP×ML) of 11×24 mm.[15]

Clinical course and follow-up: As the bridged LAD segment was superficial (1-2 mm), the consulting cardiologist did not consider it to account for the patient's atypical chest pain, and no further ischaemia testing (stress testing or invasive coronary angiography) was requested. The venous anomaly required no intervention and clinical surveillance was recommended. At one year the patient reported no recurrent chest pain or palpitations, and no atrial arrhythmia or thromboembolic event had been documented.

Case 2

A 53-year-old female was referred for CCTA after assessment for chest pain and exertional dyspnoea. She had no known cardiovascular disease and physical examination was unremarkable.

TTE showed an EF of 65%, with no valvular pathology, regional wall motion abnormality or intracardiac mass. All laboratory parameters, including cardiac biomarkers, were normal.

CCTA showed no obstructive coronary artery stenosis and was assessed as CAD-RADS 0.[14] A contrast jet consistent with a small secundum-type atrial septal defect (ASD) approximately 2 mm in diameter was identified at the mid-level of the interatrial septum (Figure 7).

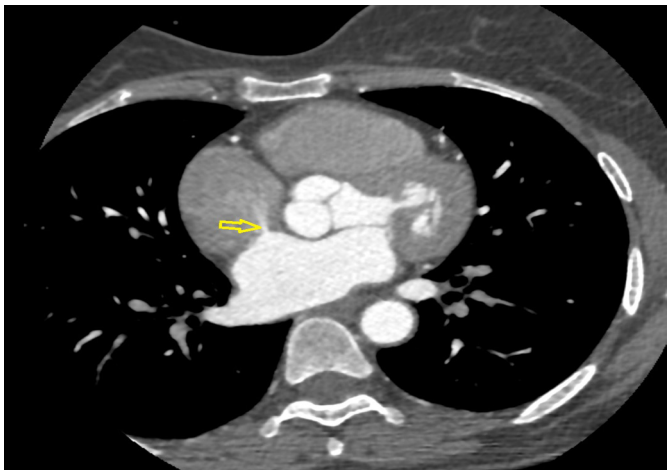

Figure 7. Case 2. Axial CT image. Yellow arrow: small secundum-type ASD
CT: Computed tomography, ASD: Atrial septal defect

Analysis of the venous system demonstrated an anomalous GCV with a tortuous course. After leaving the left atrioventricular groove the vessel passed through the space bounded anteriorly by the ascending aorta and posteriorly by the roof of the left atrium, and drained into the LAA (Figure 8-11). Because only an arterial-phase acquisition was obtained, luminal contrast filling was incomplete along the distal course of the vessel towards the interventricular septal region, so that the total length of the GCV could not be measured optimally and quantitative assessment was confined to the opacified segment. No hypoplasia, focal narrowing or interruption of the distal segment was identified; the appearance was attributed solely to suboptimal venous opacification in the arterial phase, and the

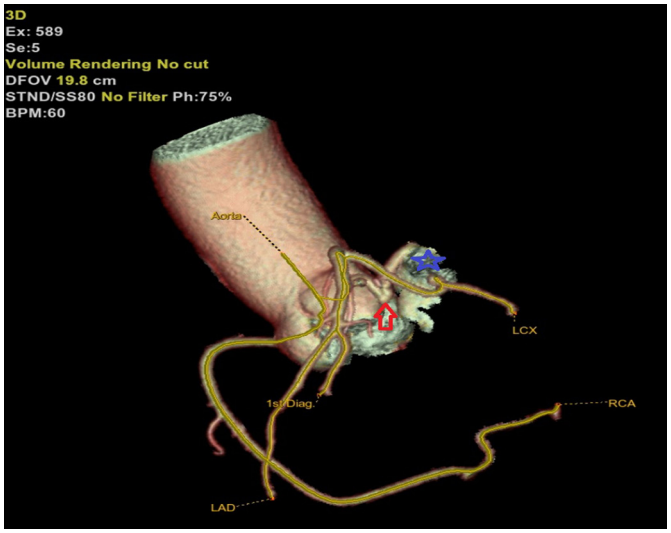

Figure 8. Case 2. Three-dimensional volume-rendered CT image. Blue star: LAA; red arrow: GCV

3D: Three-dimensional, Ex: Examination, Se: Series, DFOV: Display field of view, STND: Standard, Ph: Phase, BPM: Beats per minute, LCX: Left circumflex artery, RCA: Right coronary artery, LAD: Left anterior descending artery, Diag: Diagonal branch, CT: Computed tomography, LAA: left atrial appendage, GCV: Great cardiac vein

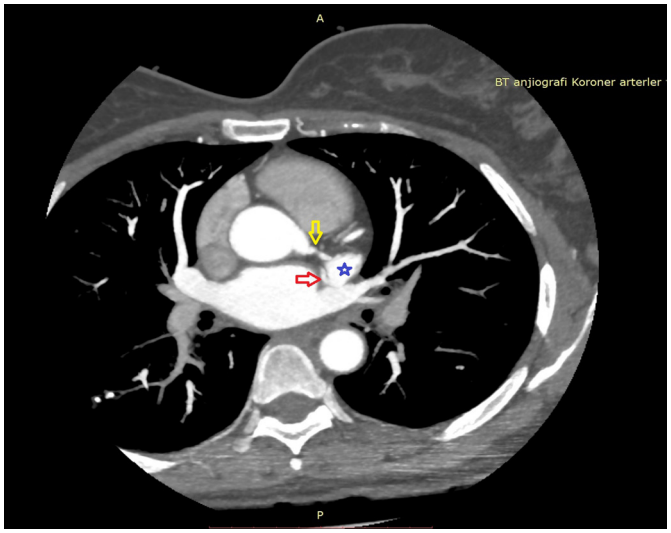

Figure 9. Case 2. Axial CT image. Blue star: LAA; red arrow: GCV; yellow arrow: left main coronary artery

CT: Computed tomography, LAA: left atrial appendage, GCV: Great cardiac vein

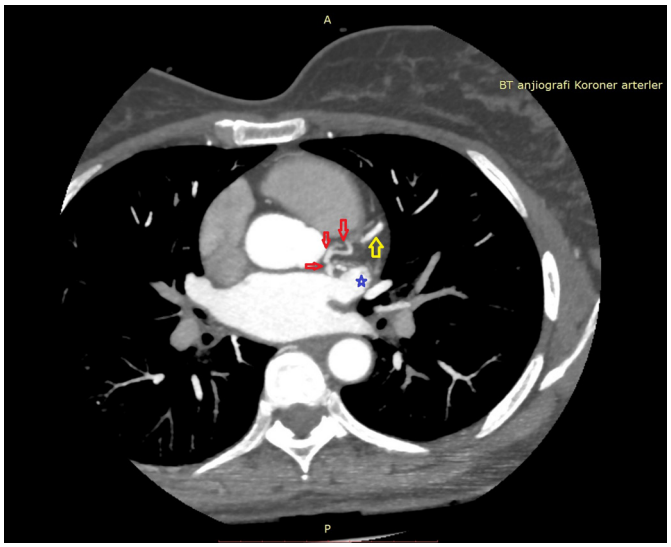

Figure 10. Case 2. Axial CT image, consecutive section following **Figure 9**. Blue star: LAA; red arrows: GCV; yellow arrow: LAD

CT: Computed tomography, LAA: left atrial appendage, GCV: Great cardiac vein, LAD: Left anterior descending artery

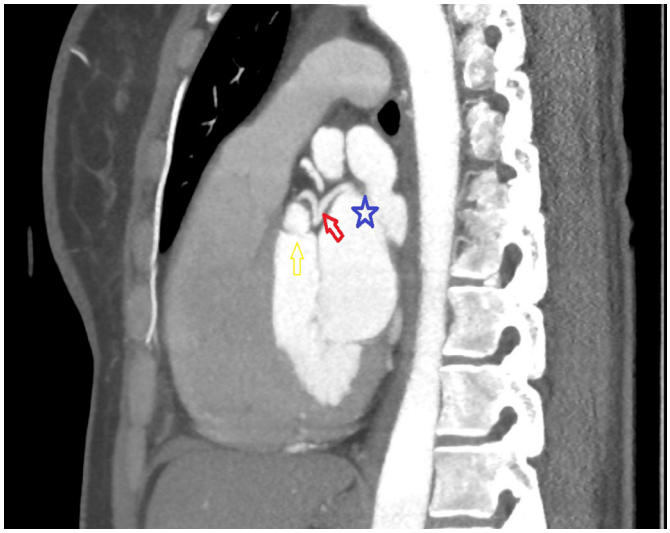

Figure 11. Case 2. Sagittal MIP CT image. Blue star: LAA; red arrow: GCV; yellow arrow: left ventricular outflow tract

MIP: Maximum intensity projection, CT: Computed tomography, LAA: left atrial appendage, GCV: Great cardiac vein

connections of the vessel with the standard venous tributaries were preserved.

A thin-walled CS, approximately 1.8 mm in diameter, was present in the posterior atrioventricular groove, with no connection to the GCV.

Quantitative measurements: The GCV measured 1.8 mm in the left atrioventricular groove and 2.4 mm immediately proximal to its termination in the LAA, and the anomalous course was 45 mm long. The LAA was of chicken-wing morphology, with maximum dimensions (AP×ML) of 12×29 mm.[15]

Clinical course and follow-up: The 2 mm secundum ASD was haemodynamically insignificant and required no intervention. As in Case 1, the patient was referred to cardiology and placed under clinical surveillance. At one year she reported no recurrent chest pain or dyspnoea, and no atrial arrhythmia or thromboembolic event had been documented. Follow-up beyond one year was not available in either patient and is acknowledged as a limitation.

DISCUSSION

Anomalous drainage of the GCV into the LAA is one of the least frequently reported coronary venous anomalies.[10-12] Yamamoto et al.[11] described a patient in whom the GCV drained into the left atrium and in whom atrial fibrillation of otherwise unexplained aetiology was present; Abazid et al.[10] reported anomalous coronary venous drainage into the left atrium detected on non-invasive imaging; and Aryal et al.[12] reported a bridging vein between the CS and the left atrium. In all of these reports the patients were adults in whom the anomaly was an incidental finding during imaging or electrophysiological study, and no consistent demographic pattern or syndromic association has emerged.

Differential Diagnosis

When a vascular structure is seen to connect with the LAA on CCTA, several entities must be excluded before a coronary venous drainage anomaly is diagnosed.

A PLSVC descends vertically anterior to the left pulmonary hilum, lateral to the aortic arch and the left pulmonary artery, and characteristically drains into a markedly dilated CS; it does not follow the atrioventricular groove and, after left-arm injection, opacifies before the right-sided structures. In both of our patients the anomalous vessel arose within the coronary venous territory, followed the atrioventricular groove and was not associated with a dilated CS.[1,2]

A left-sided or accessory pulmonary vein may lie close to the LAA and be mistaken for an anomalous vessel on volume-rendered images. Pulmonary veins can be traced peripherally into the lung parenchyma, opacify synchronously with the left atrium during pulmonary venous return and have no epicardial course within the atrioventricular groove, whereas the vessels described here could be followed along the atrioventricular groove and the course of the LAD and LCx arteries.[16]

A coronary arterial fistula arises from a coronary artery, enhances identically in timing and density to the coronary arteries, is typically dilated and tortuous, and drains into a low-pressure structure such as the right atrium, right ventricle or pulmonary artery. In our patients the anomalous vessel had no arterial origin and enhanced later and less densely than the coronary arteries, consistent with a venous structure.[17]

An arteriovenous malformation consists of a nidus of dysplastic vessels with a feeding artery and an enlarged draining vein, rather than a single, discretely traceable vessel following the course of a named cardiac vein. Neither a nidus nor early venous filling was present in either patient.[1]

Comparison of the Two Cases

The two patients shared several features: both were women in their early fifties, both were referred for CCTA because of chest pain rather than for any suspicion of a venous anomaly, neither had obstructive coronary artery disease or impaired systolic function, and in both the GCV terminated in the LAA and the anomaly remained clinically silent at one year. This concordance of gender and age is most probably a chance finding, given the very small numbers involved.

The cases differed principally in the course of the anomalous segment. In Case 1 the GCV followed an essentially normal epicardial route-along the anterior interventricular sulcus and then the left atrioventricular groove-and deviated only at its termination, so that the anomaly amounted to a distal misconnection of an otherwise normally coursing vein. In Case 2 the vessel was markedly tortuous and took an atypical route between the ascending aorta and the roof of the left atrium before reaching the LAA, so that both its course and its termination were abnormal. The incidental findings also differed: superficial myocardial bridging of the LAD in Case 1 and a small secundum ASD in Case 2.

Potential Clinical Implications

The clinical consequences of this anomaly remain theoretical, since no published case-including the two reported here-provides outcome data.

The LAA is the intracardiac structure most prone to thrombus formation, particularly in the presence of atrial fibrillation, because of its trabeculated structure and low flow velocities.[18] It has therefore been suggested that additional inflow from an anomalously draining vein might alter local flow conditions and, in theory, favour stasis and thrombus formation; this remains a hypothesis, and neither of our patients suffered a thromboembolic event during one year of follow-up.[10,18]

A relevant electrical connection between the LAA and the GCV has been demonstrated during catheter ablation of atrial fibrillation,[19] and atrial fibrillation of unexplained aetiology has been reported in a patient with anomalous GCV drainage into the left atrium.[11] Whether an anomalous GCV-LAA connection is itself arrhythmogenic cannot be determined from isolated reports, and neither of our patients had a documented atrial arrhythmia.

The implication we regard as clinically actionable is procedural: the anomaly should be recognised when planning LAA-targeted interventions, transseptal approaches and coronary sinus-related procedures.[2,4,5]

Incidental Findings

Case 1 also demonstrated myocardial bridging of the LAD. Although its length exceeded the 25 mm threshold associated with haemodynamic significance, an intramyocardial depth of less than 2 mm places the lesion in the superficial category, which carries low clinical risk.[20] No relationship between an interatrial defect, such as the small secundum ASD seen in Case 2, and anomalous GCV drainage has been described.[9] Neither finding has been reported in association with GCV-LAA drainage in the published cases.

Role of CCTA

As computed tomography technology has advanced, coronary venous anomalies have been reported with increasing frequency in the imaging literature.[2] CCTA is the preferred non-invasive imaging modality for recognising these anomalies and mapping them in three dimensions, owing to its near-isotropic high spatial resolution and to post-processing capabilities including cMPR, MIP and VR.[2,21]

This report is confined to two patients, and no inference regarding prevalence or risk can be drawn from it. The diagnosis rested on CCTA alone: neither patient underwent invasive venography, cardiac magnetic resonance imaging or electrophysiological study to confirm the connection or to establish the direction of flow. Because acquisition was optimised for the arterial phase, venous opacification was suboptimal and distal venous segments were incompletely opacified in Case 2; the total length of the GCV could therefore not be established with confidence, and the reported venous dimensions and lengths refer to the segments in which luminal contrast filling was demonstrable. CCTA also provides no information on the direction or volume of flow. Finally, follow-up was limited to one year and was based on outpatient cardiology review rather than on systematic rhythm monitoring; the longer-term follow-up required to assess thromboembolic and arrhythmic risk was not available.

CONCLUSION

In both of our patients this rare anomaly was clinically silent and required no intervention.

The individual venous trajectory should be described whenever the LAA or the coronary venous system is a procedural target. Rather than presuming an increased thromboembolic or arrhythmic risk, which the available evidence does not support, we suggest that the finding be reported descriptively and communicated to the referring cardiologist or electrophysiologist. Systematic attention to coronary venous anatomy in routine CCTA reporting, together with the accumulation of cases with adequate follow-up, offers the most realistic route to establishing the true prevalence and clinical relevance of this anomaly.

ETHICAL DECLARATIONS

Informed Consent

Written informed consent was obtained from the patients included in this report. Signed consent forms are retained by the authors and are available upon request.

Peer Review Process

This report underwent external peer review.

Conflict of Interest

The authors declare no conflicts of interest.

Financial Disclosure

This case report did not receive any financial support.

Author Contributions

Concept: MAK, AÖ; Design: MAK; Control: AÖ; Data Collection and/or Processing: MAK; Analysis and/or Interpretation: MAK, AÖ; Literature Review: MAK; Article Writing: MAK; Final Approval of the Manuscript: All Authors.

REFERENCES

1. Shah SS, Teague SD, Lu JC, Dorfman AL, Kazerooni EA, Agarwal PP. Imaging of the coronary sinus: normal anatomy and congenital abnormalities. *Radiographics*. 2012;32(4):991-1008. doi:10.1148/rg.324105220
2. Sinha M, Pandey NN, Sharma A. Anomalies of the coronary sinus and its tributaries: evaluation on multidetector computed tomography angiography. *J Thorac Imaging*. 2020;35(2):W60-W67. doi:10.1097/RTI.0000000000000456
3. Rorris FP, Katsilouli S, Bobos D, Kanakis M. Small cardiac vein draining into the inferior vena cava. *Interdiscip Cardiovasc Thorac Surg*. 2024;39(4):ivae162. doi:10.1093/icvts/ivae162
4. Habib A, Lachman N, Christensen KN, Asirvatham SJ. The anatomy of the coronary sinus venous system for the cardiac electrophysiologist. *Europace*. 2009;11 (Suppl 5):v15-v21. doi:10.1093/europace/eup270
5. Sirajuddin A, Chen MY, White CS, Arai AE. Coronary venous anatomy and anomalies. *J Cardiovasc Comput Tomogr*. 2020;14(1):80-86. doi:10.1016/j.jcct.2019.08.006
6. Anderson RH, Brown NA, Moorman AF. Development and structures of the venous pole of the heart. *Dev Dyn*. 2006;235(1):2-9. doi:10.1002/dvdy.20578
7. Gasimova NZ, Korobchenko LE, Starikova AV, et al. Role of the ligament of Marshall in arrhythmogenesis: a review. *Russ J Cardiol*. 2025;30(1):6594. doi:10.15829/1560-4071-2025-6594
8. Ojha V, Pandey NN, Sreelal TV, Gawalkar AA. Anomalous coronary venous drainage in congenitally corrected transposition of great arteries. *Heart Views*. 2025;26(3):223-225. doi:10.4103/heartviews.heartviews_71_25
9. Deniz Ç, Canpolat U. Incidental detection of coronary sinus agenesis in two patients with surgically repaired atrial septal defect. *Turk Kardiyol Dern Ars*. 2024;52(3):220-221. doi:10.5543/tkda.2023.80348
10. Abazid RM, Vezina WC, Pickering JG. Anomalous coronary venous drainage into the left atrium. *Eur Heart J Case Rep*. 2023;7(11):ytad526. doi:10.1093/ehjcr/ytad526
11. Yamamoto E, Tamura A, Kawano Y. Anomalous drainage of the great cardiac vein into the left atrium. *Circ Rep*. 2019;2(1):73-74. doi:10.1253/circrep.CR-19-0040
12. Aryal M, Neupane NP, Rajlawot K, et al. Yes, bridges do connect! A rare case of coronary sinus communicating into the left atrium through a bridging vein. *Clin Case Rep*. 2025;13(10):e70961. doi:10.1002/ccr3.70961
13. Abbara S, Blanke P, Maroules CD, et al. SCCT guidelines for the performance and acquisition of coronary computed tomographic angiography: a report of the Society of Cardiovascular Computed Tomography Guidelines Committee: endorsed by the North American Society for Cardiovascular Imaging (NASCI). *J Cardiovasc Comput Tomogr*. 2016;10(6):435-449. doi:10.1016/j.jcct.2016.10.002
14. Cury RC, Leipsic J, Abbara S, et al. CAD-RADS™ 2.0 - 2022 coronary artery disease-reporting and data system: an expert consensus document of the Society of Cardiovascular Computed Tomography (SCCT), the American College of Cardiology (ACC), the American College of Radiology (ACR), and the North America Society of Cardiovascular Imaging (NASCI). *J Cardiovasc Comput Tomogr*. 2022;16(6):536-557. doi:10.1016/j.jcct.2022.07.002
15. Di Biase L, Santangeli P, Anselmino M, et al. Does the left atrial appendage morphology correlate with the risk of stroke in patients with atrial fibrillation? Results from a multicenter study. *J Am Coll Cardiol*. 2012;60(6):531-538. doi:10.1016/j.jacc.2012.04.032
16. Porres DV, Morenza OP, Pallisa E, Roque A, Andreu J, Martínez M. Learning from the pulmonary veins. *Radiographics*. 2013;33(4):999-1022. doi:10.1148/rg.334125043
17. Yun G, Nam TH, Chun EJ. Coronary artery fistulas: pathophysiology, imaging findings, and management. *Radiographics*. 2018;38(3):688-703. doi:10.1148/rg.2018170158
18. Al-Saady NM, Obel OA, Camm AJ. Left atrial appendage: structure, function, and role in thromboembolism. *Heart*. 1999;82(5):547-554. doi:10.1136/hrt.82.5.547
19. Di Biase L, Romero J, Briceno D, et al. Evidence of relevant electrical connection between the left atrial appendage and the great cardiac vein during catheter ablation of atrial fibrillation. *Heart Rhythm*. 2019;16(7):1039-1046. doi:10.1016/j.hrthm.2019.02.009
20. Sternheim D, Power DA, Samtani R, Kini A, Fuster V, Sharma S. Myocardial bridging: diagnosis, functional assessment, and management: JACC state-of-the-art review. *J Am Coll Cardiol*. 2021;78(22):2196-2212. doi:10.1016/j.jacc.2021.09.859
21. Schertler T, Wildermuth S, Teodorovic N, Mayer D, Marincek B, Boehm T. Visualization of congenital thoracic vascular anomalies using multi-detector row computed tomography and two-and three-dimensional post-processing. *Eur J Radiol*. 2007;61(1):97-119. doi:10.1016/j.ejrad.2006.08.015